Research Square

Preprints are preliminary reports that have not undergone peer review. They should not be considered conclusive, used to inform clinical practice, or referenced by the media as validated information.

Ribs of Pinna nobilis shell induce unexpected microstructural changes that provide unique mechanical properties

Kinga Nalepka (knalepka@agh.edu.pl)
AGH University of Science and Technology https://orcid.org/0000-0002-9788-1566

Katarzyna Berent
AGH University of Science and Technology

Antonio Checa
University of Granada https://orcid.org/0000-0001-7873-7545

Tomasz Machniewicz
AGH University of Science and Technology

Adrian Harris
Micro Materials Ltd

Paweł Nalepka
AGH University of Science and Technology

Martyna Strąg
Institute of Metallurgy and Materials Science

Łukasz Maj
Institute of Metallurgy and Materials Science

Aleksandra Szkudlarek
AGH University of Science and Technology

Magdalena Bieda
Institute of Metallurgy and Materials Science

Krzysztof Sztwiertnia
Institute of Metallurgy and Materials Science

Article

Keywords: Pinna nobilis, monocrystalline, untypical

Posted Date: May 7th, 2021

DOI: https://doi.org/10.21203/rs.3.rs-51994/v2

License: This work is licensed under a Creative Commons Attribution 4.0 International License.
Read Full License

Ribs of *Pinna nobilis* shell induce unexpected microstructural changes that provide unique mechanical properties

Kinga Nalepka[1*], Katarzyna Berent[2*] Antonio G. Checa[3], Tomasz Machniewicz[1], Adrian J. Harris[4], Paweł Nalepka[1], Martyna Strąg[5], Łukasz Maj[5], Aleksandra Szkudlarek[2], Magdalena Bieda[5], and Krzysztof Sztwiertnia[5]

[1] Faculty of Mechanical Engineering and Robotics, AGH University of Science and Technology, Krakow, Poland
[2] Academic Centre for Materials and Nanotechnology, AGH University of Science and Technology, Krakow, Poland
[3] Department of Stratigraphy and Paleontology, University of Granada, Granada, Spain, and Andalusian Institute of Earth Sciences, CSIC-University of Granada, Armilla, Spain
[4] Micro Materials Ltd., Willow House, Ellice Way, Yale Business Village, Wrexham LL13 7YL, UK
[5] Institute of Metallurgy and Materials Science, Polish Academy of Sciences, Krakow, Poland

Abstract

The reinforcement function of shell ribs depends not only on their vaulted morphology but also on their microstructure. They are part of the outer layer which, in the case of the *Pinna nobilis* bivalve, is built from almost monocrystalline calcitic prisms, always oriented perpendicular to the growth surfaces. Originally, prisms and their *c*-axes follow the radii of rib curvature, becoming oblique to the shell thickness direction. Later, prisms bend to reach the nacre layer perpendicularly, but their *c*-axes retain the initial orientation. Calcite grains form nonrandom boundaries. Most often, three twin disorientations arise, with two of them observed for the first time. Nano-indentation and impact tests demonstrate that the oblique orientation of *c*-axes significantly improves the hardness and fracture toughness of prisms. Moreover, compression tests reveal that the rib area achieves a unique strength of 700 MPa. The detection of the specific microstructure formed to toughen the shell is novel.

Introduction

Bivalve shells are hierarchically complex biocomposites consisting of calcium carbonate (calcite or aragonite) and an organic matrix[1–3]. They have been improved over millions of years of

[*] Corresponding author.
E-mail address: knalepka@agh.edu.pl (K. Nalepka)
kberent@agh.edu.pl (K. Berent)

evolution to provide effective protection against predators. Consequently, the shells are lightweight and exhibit outstanding mechanical properties compared to the materials from which they are built. Thus, protective armors are an excellent source of inspiration for the formation of biomimetic engineering materials with an equally unique combination of high strength and fracture toughness[4–7]. Reproducing the shell's microstructure requires in-depth knowledge of it as well as of the mechanical properties of the components[8,9]. The present work is part of the search for engineering materials inspired by nature. The subject is a shell of the *Pinna nobilis* species with an unusual morphology due to the repair of an extensive injury that occurred at a submature stage. Thus, the examined specimen is distinguished by a large, strongly ribbed surface.

The Mediterranean pen shell *Pinna nobilis* Linnaeus, 1758 (superfamily Pinnoidea, Order Ostreida[10]) is a large endobyssate bivalve species that lives with its anterior end buried within the sediment. The shell is ornamented with radial ribs that periodically produce scales directed towards the margin (see App. A). The shell wall is made of two layers. The outer one has a columnar calcite prismatic (CCP) microstructure: large polygonal prisms elongated perpendicular to the outer shell surface, surrounded by organic sheaths. The inner layer is made of nacre, which extends for less than half the anteroposterior diameter (e.g.[1]). The two layers perform different functions. The thick (1-5 μm) periprismatic organic membranes make the outer prismatic layer particularly flexible[11]. When the two valves abut, tight sealing[12–14] is achieved by flexible deformation of the wide prismatic margins. With progressive thickening of the prismatic layer towards the apical end (up to several mm in large specimens), flexing becomes hindered and the prismatic layer exerts an armoring function. The radial ribs developed on the prismatic layer contribute to reinforcement. Given the ability of the animal to retract deeply inside the shell, damage to the margin is not lethal. The protection is provided by the tough and rigid nacre layer.

Each prismatic unit is characterized by low disorientation (the term is explained in Sec. 6) and therefore becomes a grain similar to a monocrystal (e.g.[12,13,15–17]). Previous studies on flat shell areas report that the *c*-axes of prisms remain parallel to their long axes[18–21].

The CCP layers of bivalves have been widely studied[17,22–27]. However, their mechanical properties have received little attention compared to nacre[28–31] and crossed-lamellar microstructures[32,33]. Strąg et

al.[34] reported values of 460 MPa and 3.86 GPa for the compressive strength and nanohardness of the calcitic layer of *Pinctada margaritifera*, respectively. Kunitake et al.[35] showed that the hardness of the *Atrina rigida* CCP layer varies with the rotation of the indenter tip around the normal to the loaded *c* plane. Accordingly, the range of 3.47–4.19 GPa was obtained at a penetration depth of 170 nm. A similar dependence was found in *Pinna nobilis*: 3.89–4.86 GPa at a variable indentation depth of 100–250 nm[36].

The aim of this study is to accurately characterize the CCP microstructure of *P. nobilis* in the areas of ribs and link it with the mechanical properties of the constituent elements as well as with the response to load of a representative volume. A specimen with a large, densely ribbed surface was used, shaped by extensive damage in the early stage of growth. Investigations with application of the electron backscatter diffraction (EBSD) method have revealed unusual orientations of prismatic calcite grains, which play a key role in transferring the external load. This was demonstrated through theoretical analysis and then confirmed by the identification of mechanical properties at the local and global levels with nano-indentation, nano-impact and compression tests.

Microstructure identification

The studied shell has a morphology unusual for the *P. nobilis* species (compare App. A). A clear division line running longitudinally on both valves is visible (Fig. 1a). The reason is breakage of the shell at a submature stage of growth. The trace of the former fracture begins with a clear notch separating the posterior of the primary shell from the restored area. The further course of the crack is determined, on the external surface, by the discontinuity of the ribs, which are distributed more densely in the repaired part. In the same area, there is a thick nacre coating on the inside. After breaking, the shell was rebuilt asymmetrically. The dorsal and ventral parts developed independently. The first of them underwent significant expansion. In spite of the bilobate appearance, the examined shell preserves the geometric structure of the surface characteristic for the *P. nobilis* species. Its key component is the waviness generated by ribs running in the radial direction (Fig. 1b-e). They are formed by periodically distributed segments of mantle specialized for the production of ribs. Upon growth, segments move along radial trajectories, thus producing a series of radial ribs[37]. The waviness integrally inscribed in the

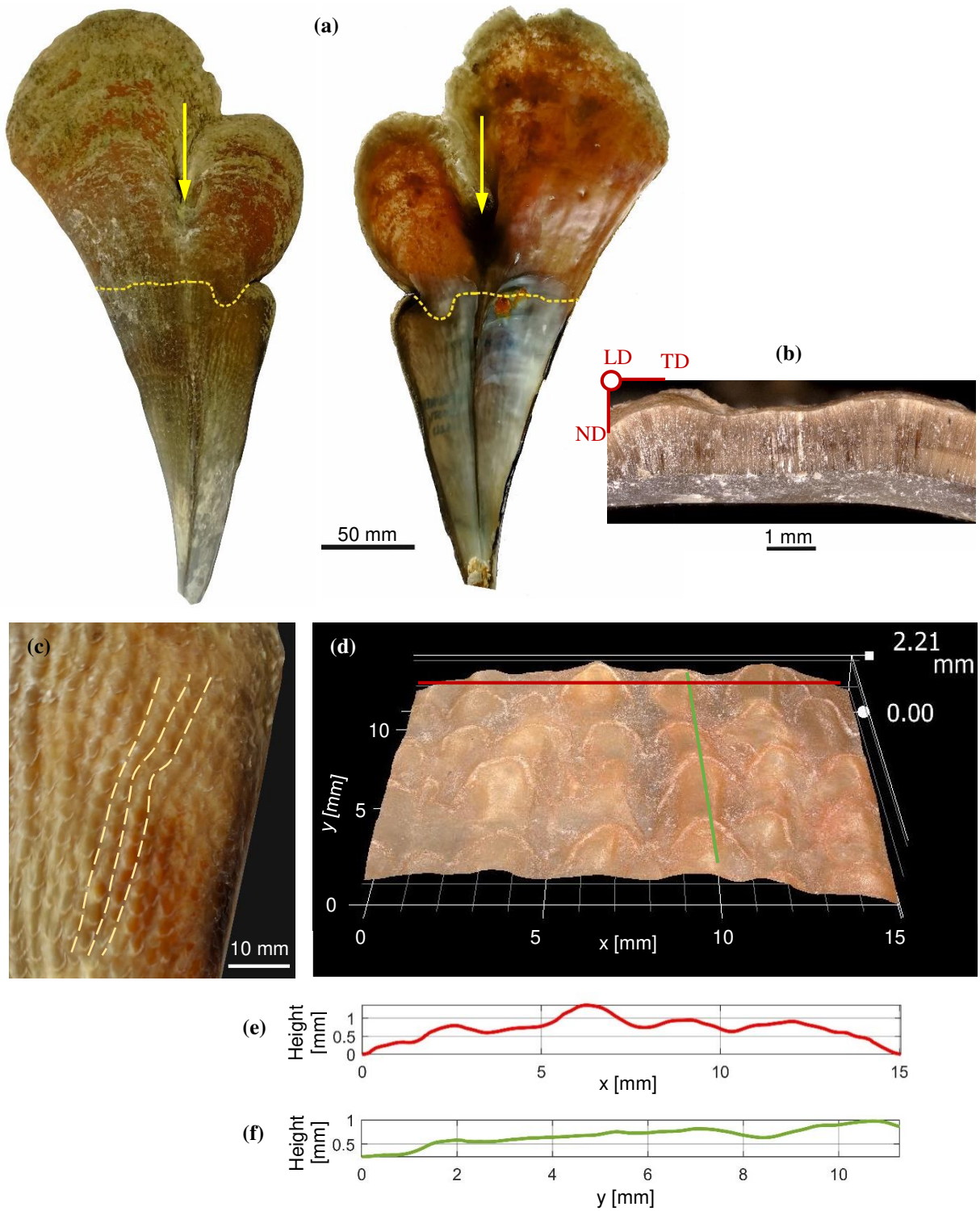

Fig. 1 Morphology of *Pinna nobilis* shell. (a) Outer and inner view of the left valve of the specimen showing the bilobate margin produced by shell repair. The trace of the former fracture is marked with a broken yellow curve and the division lines of valves are indicated by arrows. (b) Cross-section of the shell determined by normal (ND) and transversal (TD) directions. (c) Ribs in the ventral part. Three of them are distinguished by broken yellow lines. (d) Surface with profiles measured along (e) transversal (TD) and (f) longitudinal (LD) directions.

three-dimensional surface topography induces a specific microstructure of the shell's cross-section. In order to identify it, in-depth EBSD investigations were carried out.

Prisms, growing perpendicularly to the undulated outer surface, deviate from the normal direction (ND) determined by the shell thickness. As a result, in the outer layer, the directions of fast growth, i.e. *c*-axes of calcite grains, are mostly oblique (Fig. 2). With shell thickening, growth lines become flatter and the orientation of the growth axes of prisms becomes more and more parallel to ND. This process leads to the deflection of prisms as well as to elimination of those that exhibit a significant initial deviation from the normal direction (Fig. 2a).

The ordered orientation of prisms does not mean that it is preserved by calcite grains. It turns out that, during the growth of grains, the *c*-axes maintain their initial direction. As a result, obliquely initiated orientation becomes obligatory throughout the entire thickness of the shell. Thus, the wavy surface determines the texture of the entire protective armor. Analysis of the EBSD results reveals a clear division into three areas. Both the outer surface profile and the growth lines indicate that these regions correspond to three adjacent ribs running perpendicular to the image in the longitudinal direction (LD) (see Fig. 2a). The middle area is initiated by a local shell elevation with a small curvature, while the lateral ones begin with a greater slope. As a result, in the central region, the *c*-axes of prisms are most frequently tilted by a small angle of 12° relative to ND, and their initial orientation is maintained up to the nacre layer (Fig. 2b, compare red and black plots). The central area is flanked by two half ribs with a higher curvature, particularly the left one. Hence, in their upper parts, the *c*-axes of grains most often orientate at an angle of 32° (left rib) and 14° (right rib) relative to ND (Fig. 2b, red plot). The organization of both zones is similar. Initially, grains with an oblique inclination tend to disappear, whereas their neighbors expand at their expense. In this way, grains with *c*-axes significantly deviated from ND are eliminated, while those which form a group with a similar orientation of *c*-axes reach the nacre layer. The grains G1 and G2 are perfect examples. The first one exhibits the deviation angle of 15°, preferred in the right rib area. The other one has a much larger angle of 23°. Finally, G1 reaches the nacre layer while G2 vanishes. Even its sudden deflection causes only a slight change in the orientation of calcite - the difference remains within 2°.

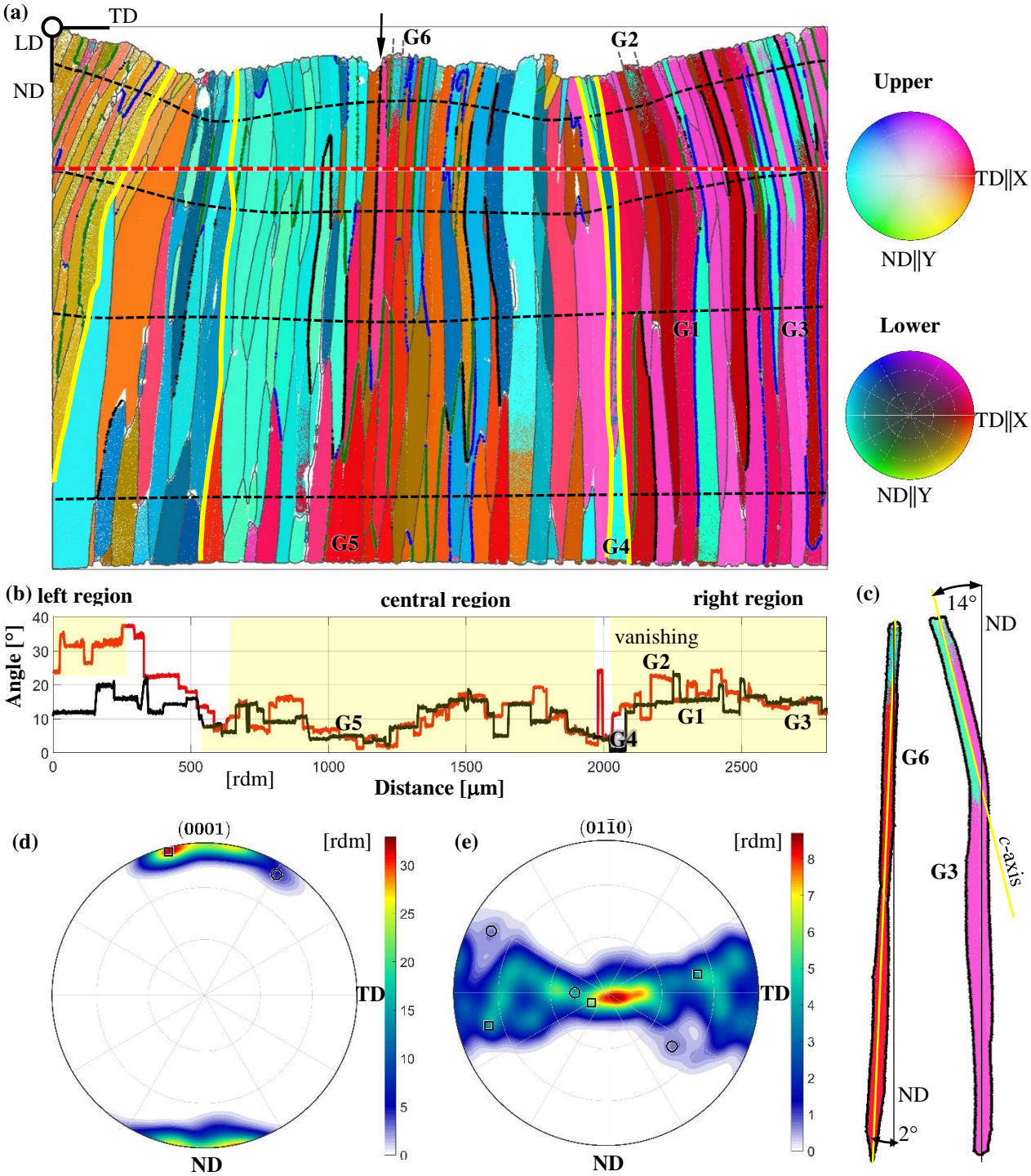

Fig. 2 Microstructure of a representative cross-section through a ribbed area. (a) Orientation in axis/angle color coding. The color determines the position of the axis, while the angle of rotation is expressed by the color saturation, 0° and 90° correspond to gray and full saturation, respectively. Grains typical of *P. nobilis*, with the axis *c* subparallel to ND, are generated through an axis with a red (e.g. G4) or blue pole (e.g. G5). Then the rotation by 90° moves the *c*-axis to the ND position. The regions with distinct microstructures are separated by yellow lines whereas the trace of a morphological symmetry plane is indicated by an arrow. The growth lines are denoted by black dashed lines, while boundaries with the specific disorientations A, B, C are marked in green, blue and black. (b) Angle of deviation of the *c*-axis from ND depending on the position determined by the level of the second (red) and the last (black) growth line. (c) Examples of grains: typical of *P. nobilis* and deflected. In the first case, *c*-axis (yellow) is subparallel to ND (d), (e) Pole distribution function (PDF) for {0 0 0 1} and {0 1 $\bar{1}$ 0} planes together with the most frequent orientations in the left (circle) and right (square) region.

The question arises as to whether there is a preference in the mutual orientation of adjacent grains. The calculated Misorientation Distribution Function (MDF) shows that the grains rotate with respect to each other around the *c*-axis, taking three preferential positions. They are determined by the following values of the rotation angle ω: 18° (A), 38° (B) and 60° (C) (Fig. 3a). High preference is usually due to the system's striving to the formation of low-energy boundaries. Hence, we conducted calculations to reveal how interfacial energy changes when adjacent calcite crystallites are rotated around the *c*-axis. Accurate determination of the quantity for the continuous rotation is virtually impossible due to the excessively high computational cost. Therefore, an approximated method developed by Gautam and Howe[38] is used. According to it, interfacial energy decreases with the increase

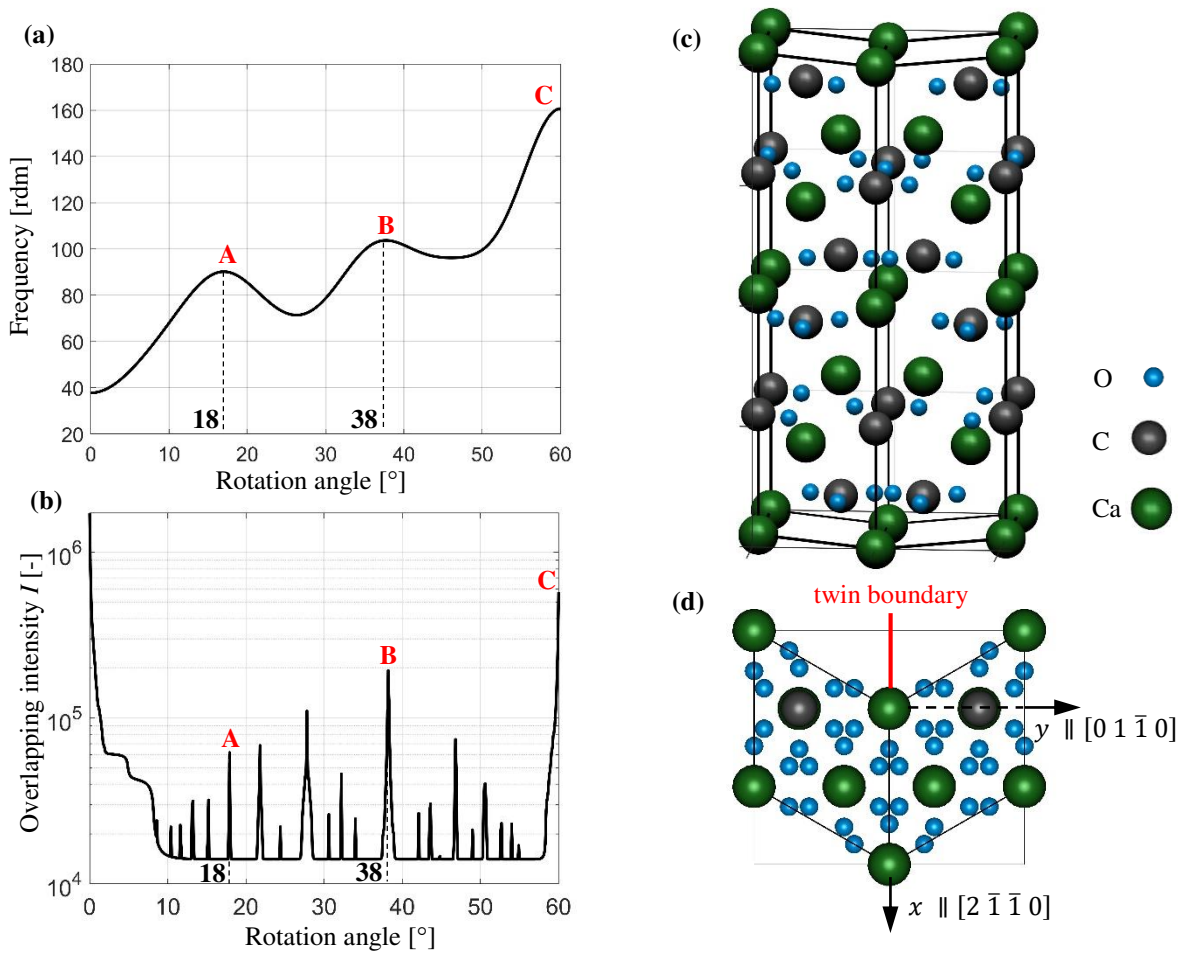

Fig. 3 Preference in the misorientation of grains. (a) Distribution of disorientation angle for rotation about the *c*-axis showing three preferred disorientations between calcite grains of the cross-section (A, B, C) (b) Dependence of overlapping intensity *I* on the disorientation angle of rotation around the *c*-axis. The local maxima determine low-energy disorientations. (c), (d) $(0\ 1\ \bar{1}\ 0)$ calcite twin.

of the total intensity *I* contained in the areas of overlapping diffraction reflections from neighboring

crystallites. Thus, using the last quantity we can find disorientations, to which local energy minima correspond (see Sec. 6).

The results clearly show that strictly defined low-energy boundaries, i.e. rotation angles, are preferred (Fig. 3b). Particularly important is the disorientation described by the 60° rotation about the *c*-axis. Two symmetrically equivalent orientation relationships correspond to it. They constitute two twin boundaries formed by the reflection planes $(0\ 1\ \bar{1}\ 0)$ and $(0\ 0\ 0\ 1)$, respectively. The prismatic structure, whose elements mostly run through the entire thickness of the shells, means that the first of them mainly occurs. The twin boundary $(0\ 1\ \bar{1}\ 0)$, positioning perpendicular to the growth line, allows it to be curved, because the crystallographic plane terminating the growth stage is mirrored to the adjacent area (comp. Fig. 3c, d and Fig. 4a, b). As a result, grains separated by a morphological plane of symmetry form a coherent connection. Another example is the boundary running along the symmetry axis of the central region (indicated by the arrow in Fig. 2a). The other preferred disorientations are also generated by twin relationships, but this time the mirror planes have higher indices $(1\ \bar{5}\ 4\ 0)$ and $(4\ 7\ \overline{11}\ 0)$ for 38° and 18°, respectively. These two uncovered twin relations are formed between grains of biogenic calcite thanks to the presence of biomolecules. They define new, hitherto unknown, orientation relationships that are highly prevalent in *P. nobilis* shells. The preferences observed experimentally are justified by the theoretical analysis of the misorientation space of a calcite crystal.

Something that could be of interest is how twin relationships can exist when monocrystalline prisms are separated by thick organic membranes. Checa et al.[26] showed how new membranes are introduced very early during the growth of prisms in the CCP layers of several pterioids, thus dividing otherwise continuous crystalline domains. We can hypothesize that the low-energy disorientations were formed in initial growth stages in *Pinna* and twinned grains were later separated by membranes. Given the low disorientations recorded in *Pinna* prisms, grains remained in the twin relationship long after they were separated by membranes.

The EBSD investigations performed for the representative fragment of the shell surface confirm that the waviness leads to calcite prism inclination (Fig. 4). The *c*-axes oriented perpendicular to the curved surface assume four preferential positions. This is revealed by the pole distribution function

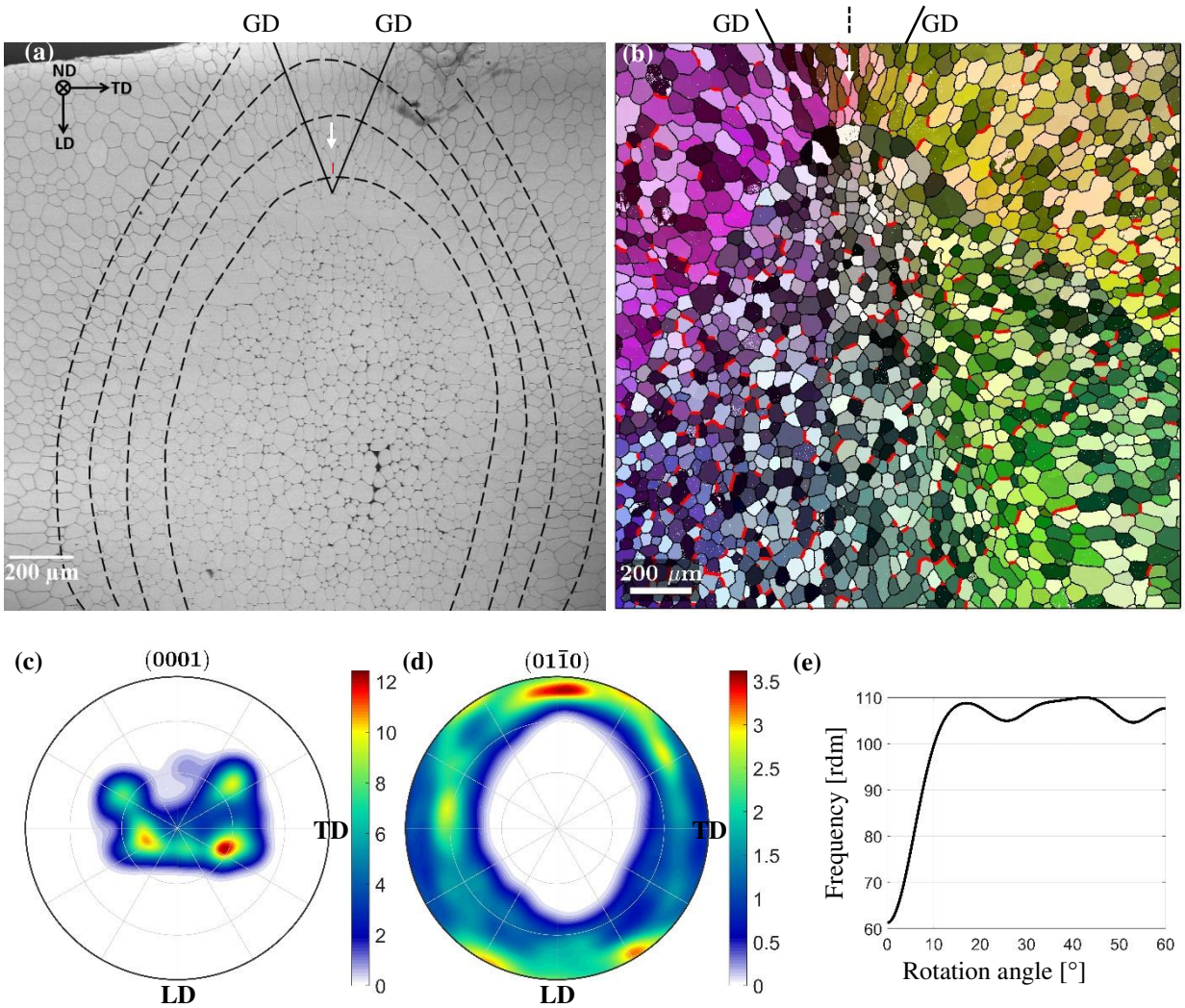

Fig. 4 Microstructure of the outer shell surface. (a) SEM image with growth lines denoted by black dashed lines. (b) Grain orientation in axis/angle colour coding. Twin boundaries $(0\ 1\ \bar{1}\ 0)$ are marked in red. One of them providing a smooth change in the growth direction (GD) is indicated by a white arrow. (c), (d) PDF for $\{0\ 0\ 0\ 1\}$ and $\{0\ 1\ \bar{1}\ 0\}$ planes. (e) Distribution of disorientation angle for rotation about *c* axis.

(PDF) whose four maxima show that *c*-axes deviate from ND by 26°, 16°, 38°, and 36°, respectively (Fig. 4c). The identified orientations of *c*-axes reflect the microstructure division into regions in which grains start to grow from differently sloping surfaces. The four zones formed are clearly depicted by means of axis/angle color coding (Fig. 4b). Both calcite grains situated along ND, as well as those inclined rotate around their *c*-axes, showing a tendency to locate the planes {0 1 -1 0} perpendicular to the longitudinal direction (Fig. 4d). Actually, the rotation is continuous, so there are not clear angular preferences (Fig. 4e). We can say, that in the initial growth stage, the disorientation of prisms is largely random. With shell development, low-energy boundaries are continued and others tend to disappear.

This is shown by the results obtained for the cross-section (Fig. 3a, b). The surface image captures the area of elongated grains, whose longer boundaries are determined by the directions of growth. At the place of strong curvature in the growth line, they deviate from each other. This is enabled by the twin boundary that runs along the longitudinal direction (LD) (comp. Fig. 3d and Fig. 4a, b). In this way, the mirror symmetry between adjacent grains is combined with the symmetry of the entire area morphology.

The question arises as to how the microstructure induced by ribs affects the mechanical properties of the material. In order to solve the problem posed, research was carried out at different levels of the scale. In the first stage, static and dynamic nano-indentation of prisms with various orientations was performed. Then, we conducted static compression tests of cubic elements representing rib areas with strongly inclined *c*-axes.

Nano-indentation tests

Theoretical analysis

Calcite anisotropy makes prism orientation a key determinant of global mechanical properties. The arrangement of these basic structural units controls the activation and course of plastic deformations, brittle fracture processes as well as their mutual coupling.

Experiments carried out for the geological single calcite crystal have identified two basic mechanisms of glide *r* $\{0\,\bar{1}\,1\,4\}\langle 0\,2\,\bar{2}\,1\rangle^{\pm}$, *f* $\{\bar{1}\,0\,1\,2\}\langle 2\,\bar{2}\,0\,1\rangle^{\pm}$ and one of twinning *e* $\{\bar{1}\,0\,1\,8\}\langle 4\,0\,\bar{4}\,1\rangle^{+}$. At room temperature, despite the high pressure caused by indentation, not all slip systems are activated, but only three out of six of each type: *r* $\langle 0\,2\,\bar{2}\,1\rangle^{-}$, *f* $\langle 2\,\bar{2}\,0\,1\rangle^{-}$. Of course, this depends on the resolved shear stress operating in a given slip system. The lowest critical value of 110 MPa was identified for the *r* planes[39]. Hence *r* $\langle 0\,2\,\bar{2}\,1\rangle^{-}$ slips play a key role in the plastic deformation of calcite grains. The resolved shear stress can be determined by the Schmid factor *S* according to the relationship: $\tau = \sigma_0 S = \sigma_0 \cos\varphi \cos\lambda$, where σ_0 is normal stress on the indented surface, while φ and λ are angles between the loading direction and the normal of a slip plane $\hat{\boldsymbol{n}}$ or a slip direction $\hat{\boldsymbol{s}}$, respectively. The Schmid factor depends on the orientation of a grain and the slip system that is activated inside it. If we assume an initial reference system with the *z* axis parallel to the loading direction (see

Fig. 5a) and a final one determined by the system of a rotated crystal $\hat{\boldsymbol{x}}_{\boldsymbol{c}} \parallel [2\,\bar{1}\,\bar{1}\,0], \hat{\boldsymbol{y}}_{\boldsymbol{c}} \parallel [0\,1\,\bar{1}\,0], \hat{\boldsymbol{z}}_{\boldsymbol{c}} \parallel [0\,0\,0\,1]$ (Fig. 5), then the considered coefficient can be expressed by Euler angles and coordinates of unit vectors of the analyzed slip system $\hat{\boldsymbol{n}}$ and $\hat{\boldsymbol{s}}$. As a result, we obtain the following formula:

$$S = \left(n_x \sin\varphi_2 \sin\Phi + n_y \cos\varphi_2 \sin\Phi + n_z \cos\Phi\right)\left(s_x \sin\varphi_2 \sin\Phi + s_y \cos\varphi_2 \sin\Phi + s_z \cos\Phi\right) \quad (1)$$

The relation is depicted for those slip systems that give the highest values of the Schmid factor in the case of indented grains (Fig. 6a-c). A positive sign of the quantity means agreement between the signs of the applied normal stress and the resulting slip in the considered system.

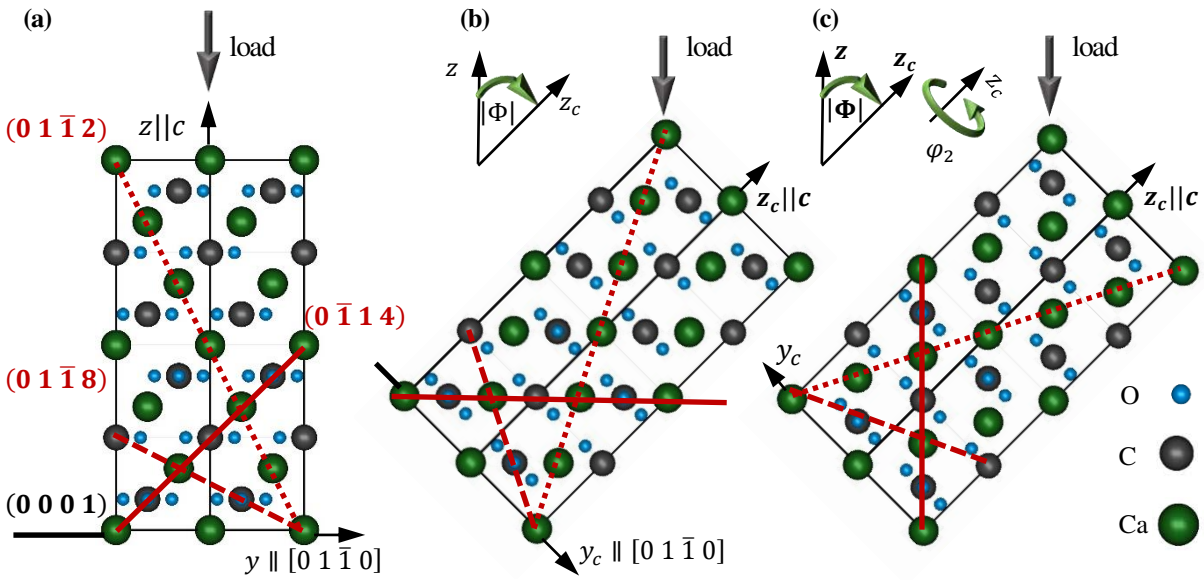

Fig. 5 Typical and inclined grains. (a) Two calcite elementary cells at the initial position (b) and after rotation by the angle $\Phi = -45°$, which is equivalent to $\Phi = 45°, \varphi_2 = 60°$ in an asymmetric domain of the orientation space. (c) Twin of the crystal (b), $\Phi = -45°, \varphi_2 = 180°$, which is equivalent to $\Phi = 45°, \varphi_2 = 0°$ in an asymmetric domain. The planes for plastic and brittle deformation are also depicted.

Ionic bonding of calcite makes it prone to brittle fracture. The key cleavage planes are $\{0\,\bar{1}\,1\,4\}$. Separating a unit area of such a surface from the bulk crystal requires relatively little work, i.e. surface energy γ_{CP}. Subsequent cleavage planes with higher surface energy are $\{\bar{1}\,1\,0\,\bar{8}\}$ and $\{0\,0\,0\,1\}$. The classification presented is based on the results obtained by Bruno et al.[40] using the molecular dynamics method. According to their calculations, the relaxed surface energy at 0 K for individual planes is 0.534, 0.702 and 0.711 J/m^2, respectively. Fracture in a given plane requires appropriate normal stresses. They arise during nano-indentations at the unloading stage. Their value can be calculated on the basis of simple geometrical relationships if we assume that there is a one-dimensional stress state σ_0 under the

indenter: $\sigma = \sigma_0 cos^2\varphi = \sigma_0 C$. Thus, the amount of tensile stress on a given plane is determined by the cleavage factor C. Its value depends on coordinates of a unit vector normal to the plane and Euler angles that orientate an intended grain. This is expressed by the following formula:

$$C = \left(n_x \sin\varphi_2 \sin\Phi + n_y \cos\varphi_2 \sin\Phi + n_z \cos\Phi\right)^2 \quad (2)$$

The relation is illustrated for three planes representing the mentioned families. The chosen planes generate the highest values of the factor in the case of intended grains (Fig. 6d-f).

Prisms typical of the *Pinna nobilis* species with the *c*-axes running along the shell's thickness (ND) (Fig. 5a) are not the best mechanical solution. Then, regardless of the rotation of the grain around the *c*-axis, a maximal resolved shear stress equal to half the compressive stress applied to the outer surface is generated in the $(0\ \bar{1}\ 1\ 4)[0\ 2\ \bar{2}\ 1]^-$ system (Fig. 6a). Thus, in a given orientation of the prism, slips can be activated in three planes $\{0\ \bar{1}\ 1\ 4\}$ simultaneously. Similarly, basic twin systems $\{\bar{1}\ 0\ 1\ 8\}\langle 4\ 0\ \bar{4}\ 1\rangle^+$ achieve a high Schmid factor exceeding 0.4 (Fig. 6b). They are activated during unloading. As a result, grains typical of *Pinna nobilis* undergo intensive plastic deformations. Moreover, there is a possibility of fracture along the $\{0\ 0\ 0\ 1\}$ plane because, during unloading, tensile stresses are perpendicular to it (Fig. 6f).

Geometric analysis of plastic processes shows that the inclination of grains significantly improves their mechanical properties. Due to the deviation of the *c*-axis from the outer surface normal, the systems of easy slips are so-oriented that the formation of shear stresses necessary to induce permanent deformations is difficult. As the angle Φ increases, the factor S of the slip family $\{0\ \bar{1}\ 1\ 4\}\langle 0\ 2\ \bar{2}\ 1\rangle$ decreases (Fig. 6a). Thus, during loading, the key glide mechanism $r\ \langle 0\ 2\ \bar{2}\ 1\rangle^-$ is confined. At an appropriately high stress, the single system $(0\ 1\ \bar{1}\ 2)[2\ \bar{2}\ 0\ 1]^-$ is activated. Initially, it is constrained to a small group of grains with orientations near the (49°, 35°) point, which constitutes the maximum Schmid factor (Fig. 6c). It is worth noting that, at the same time, in other systems of this family, the S coefficient does not exceed 0.13. At the unloading stage, the glide mechanism $r\ \langle 0\ 2\ \bar{2}\ 1\rangle^-$ is not activated at all. Instead, in the single systems $(\bar{1}\ 0\ 1\ 8)[4\ 0\ \bar{4}\ 1]^+$ and $(\bar{1}\ 1\ 0\ \bar{2})[0\ 2\ \bar{2}\ 1]^-$, twinning and slipping occur respectively. Starting the last process is identified by the Schmid factor, which at the point (71°, 35°) reaches the minimal value -0.5.

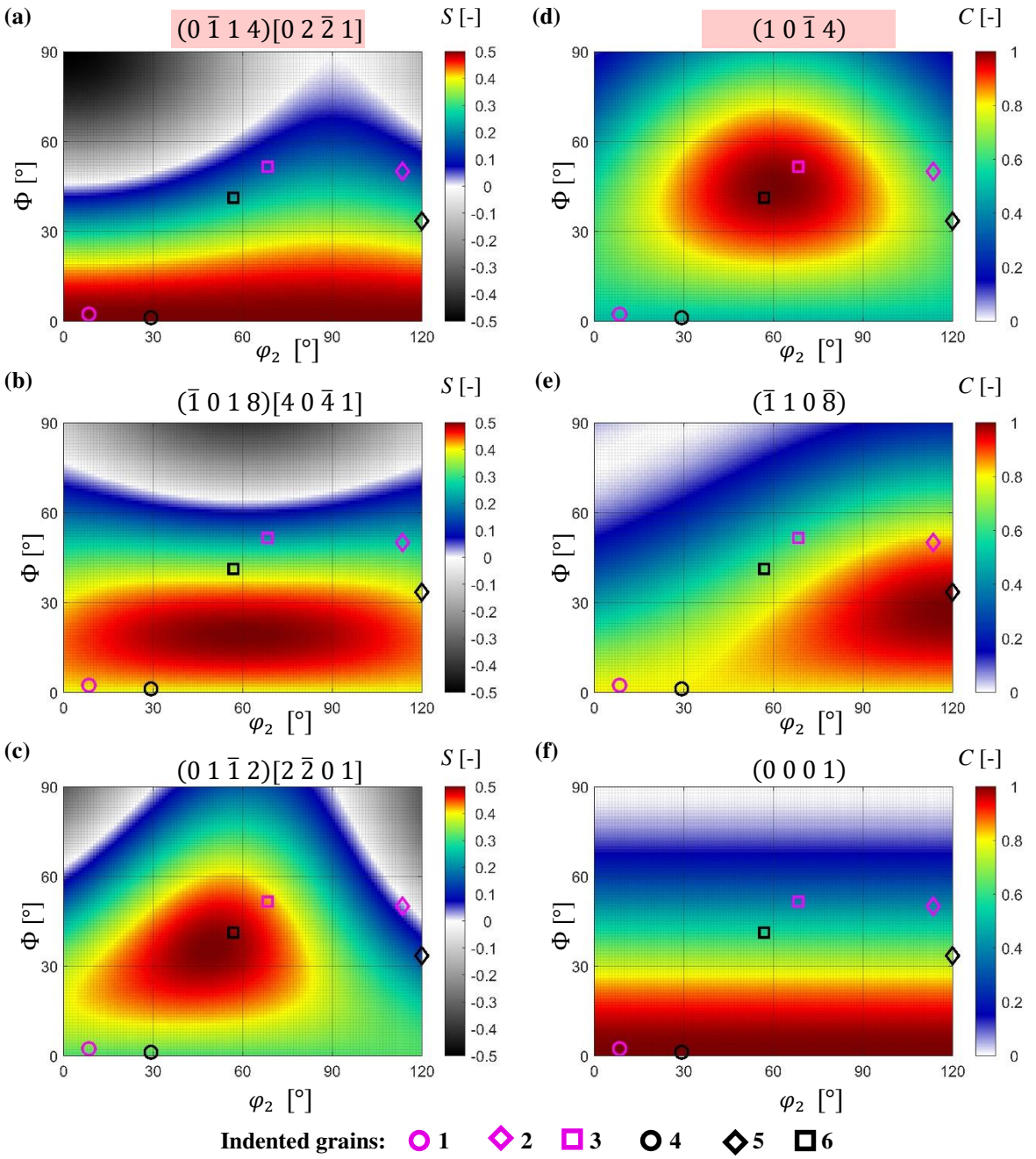

Fig. 6 Schmid factor *S* and cleavage factor *C* for representative slip systems and fracture planes as functions of the crystal orientation determined by Euler angles. The relationships are presented for those slip systems and cleavage planes at which the coefficients achieve the highest values in indented grains 1–6. A positive *S* factor means that during unloading a positive slip arises, while at the loading stage a negative slip is generated.

Thus, with a relatively low external load, the glide processes inside typical grains are activated. When the prisms deviate from ND above 30°, the initiation of slips requires the application of higher normal stresses to the outer surface. Then confined plastic deformations will occur in the systems *r* $\langle 0\,2\,\bar{2}\,1\rangle^{-}$, and in grains with a specific orientation will continue in the single system

$(0\ 1\ \bar{1}\ 2)[2\ \bar{2}\ 0\ 1]^{-}$. Thus, the degree of permanent deformation is lower. In the case of engineering materials, an increase in strength is associated with a decrease in fracture toughness. This relationship also affects the *Pinna nobilis* protective armor but is limited to a small group of grains with specific orientations determined by Euler's angles from the vicinity of the (60°, 45°) point (Fig 6d). Then the plane of easy cleavage $(1\ 0\ \bar{1}\ 4)$ is located perpendicular to the normal force acting on the outer surface (see Fig. 5b). Hence, during unloading, an extensive crack will form. Other grains tend to split along the planes $\{\bar{1}\ 1\ 0\ \bar{8}\}, \{0\ 0\ 0\ 1\}$. Then, separation requires higher energy. Hence, the fracture process is initiated at a higher load and is often combined with plastic deformation, which limits the crack growth. To sum up, the anisotropy of calcite crystal makes the inclined prisms show higher strength and fracture toughness in comparison to those with *c*-axes parallel to ND. An exception is a small group in which the planes $\{1\ 0\ \bar{1}\ 4\}$ orientate perpendicular to ND. Nevertheless, the twin boundary $(0\ 1\ \bar{1}\ 0)$ transforms the grains into the adjacent ones which show significantly higher strength and toughness (Fig. 5c).

Experimental results

The regularities revealed in the theoretical analysis are mapped by the relation that combines the values of the mechanical property measured for representative grains in the nano-indentation test. Two groups were studied, each of which consists of three grains (see App. B). The first prism preserves the *c*-axis parallel to ND, the second one shows a strong inclination, while the other due to the specific tilting has a plane $\{1\ 0\ \bar{1}\ 4\}$ oriented perpendicular to ND with an accuracy of 10°. Schmid and cleavage factors for individual grains are presented in previously prepared distributions (Fig. 6). The first prism exhibits the lowest hardness, the second one, the highest, and the third one is characterized by an intermediate value (Tab. 1). The obtained maps show that the response of the second grain is largely uniform, while that of the first one is varied. A large part of prism 1 exhibits a hardness at a low level of 3.0 GPa (Fig. 7c, d). The higher average value results from locally occurring harder areas. Research conducted on biogenic calcite shows that one of the sources of improving mechanical properties is structural defects[35].

Table 1 Mechanical properties of the shell's grains

Grain	Hardness [GPa]	Reduced elastic modulus [GPa]
1	3.26 ± 0.38	66.8 ± 4.8
2	3.55 ± 0.34	66.4 ± 4.2
3	3.44 ± 0.34	75.1 ± 5.3

The experimental results confirm the theoretical predictions. Grains typical for *Pinna nobilis* easily undergo plastic deformation. Inclination significantly hinders these processes, which induces the increase in hardness.

Interestingly, the values of elastic modulus are ordered in a different way. The grain with the medium hardness attains the highest stiffness of 75.1 GPa. The reason is the densely packed plane which is located almost perpendicular to the load direction. This grain forms a disorientation, close to the twin relationship with respect to the plane $(0\ 1\ \bar{1}\ 0)$, with the adjacent grain, number 2. The rotation that occurs then causes the plane $(1\ 0\ \bar{1}\ 4)$ to be almost vertical, i.e. parallel to ND. As a result, the mechanical response is determined by a random plane with high indices. Its rare packing makes the elastic modulus the lowest. The orientations of prisms 3 and 2 are similar to those shown in Fig. 5. The first of these grains exhibits the maximal cleavage factor for the key plane $(1\ 0\ \bar{1}\ 4)$. The other one, due to the disorientation close to the twin relationship, reduces this coefficient to 0.

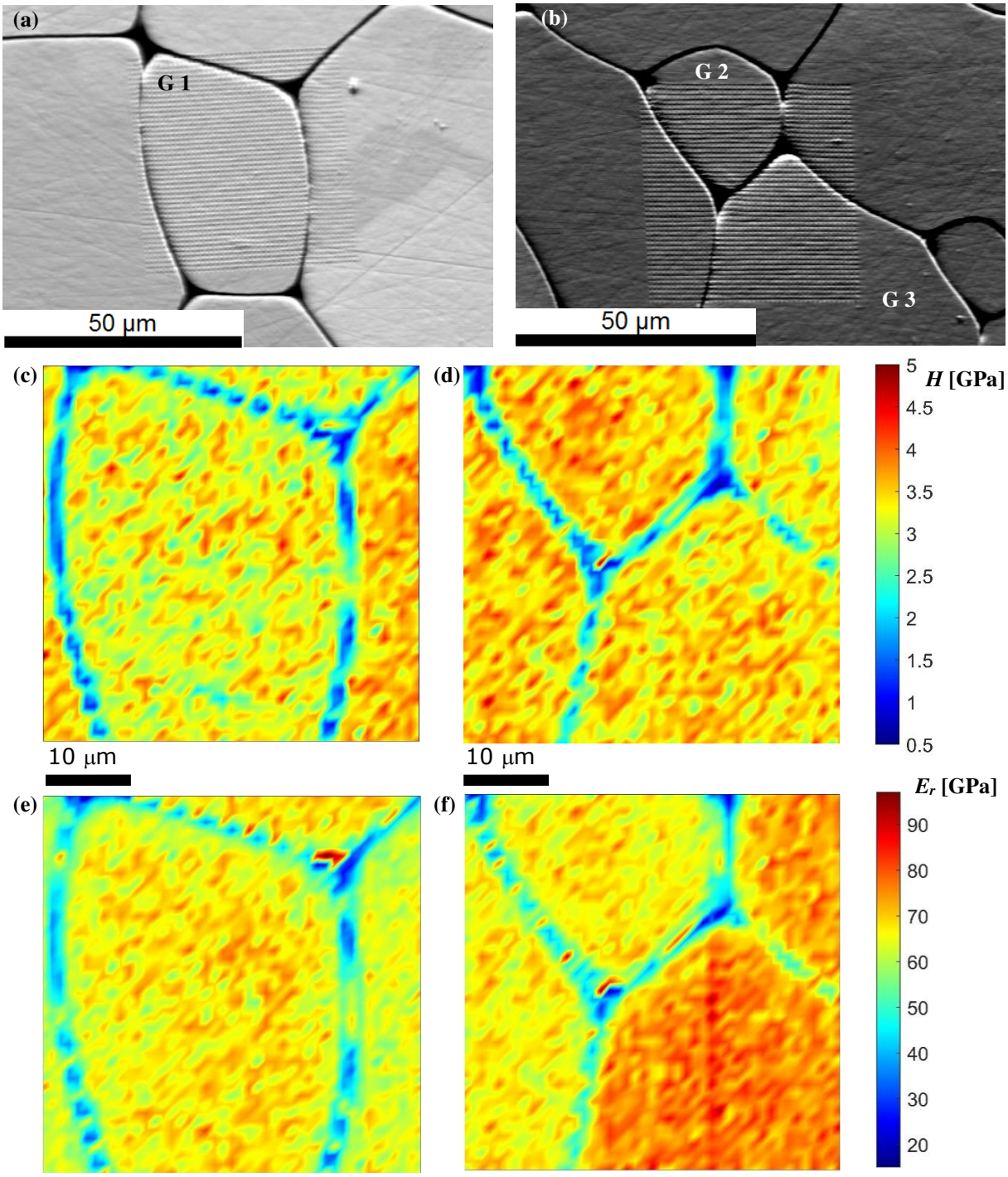

Fig. 7 Nano-indentation results on individual grains. (a), (b) SEM images of the indented areas. (c), (d) hardness distribution. (e), (f) reduced elastic modulus distribution.

Additional information on how the orientation of the grains controls the mechanical properties is provided by the second group of grains subjected to the impact test (see App. B). Most cracks are formed in prism 4, with its *c*-axis subparallel to ND, typical for *Pinna nobilis* shells (Fig. 8a). They develop in a radial direction from the corners of the impression or along the traces of planes {1 0 -1 4}. The reason is significant plastic deformation caused at the loading stage. As in the case of the indentation of

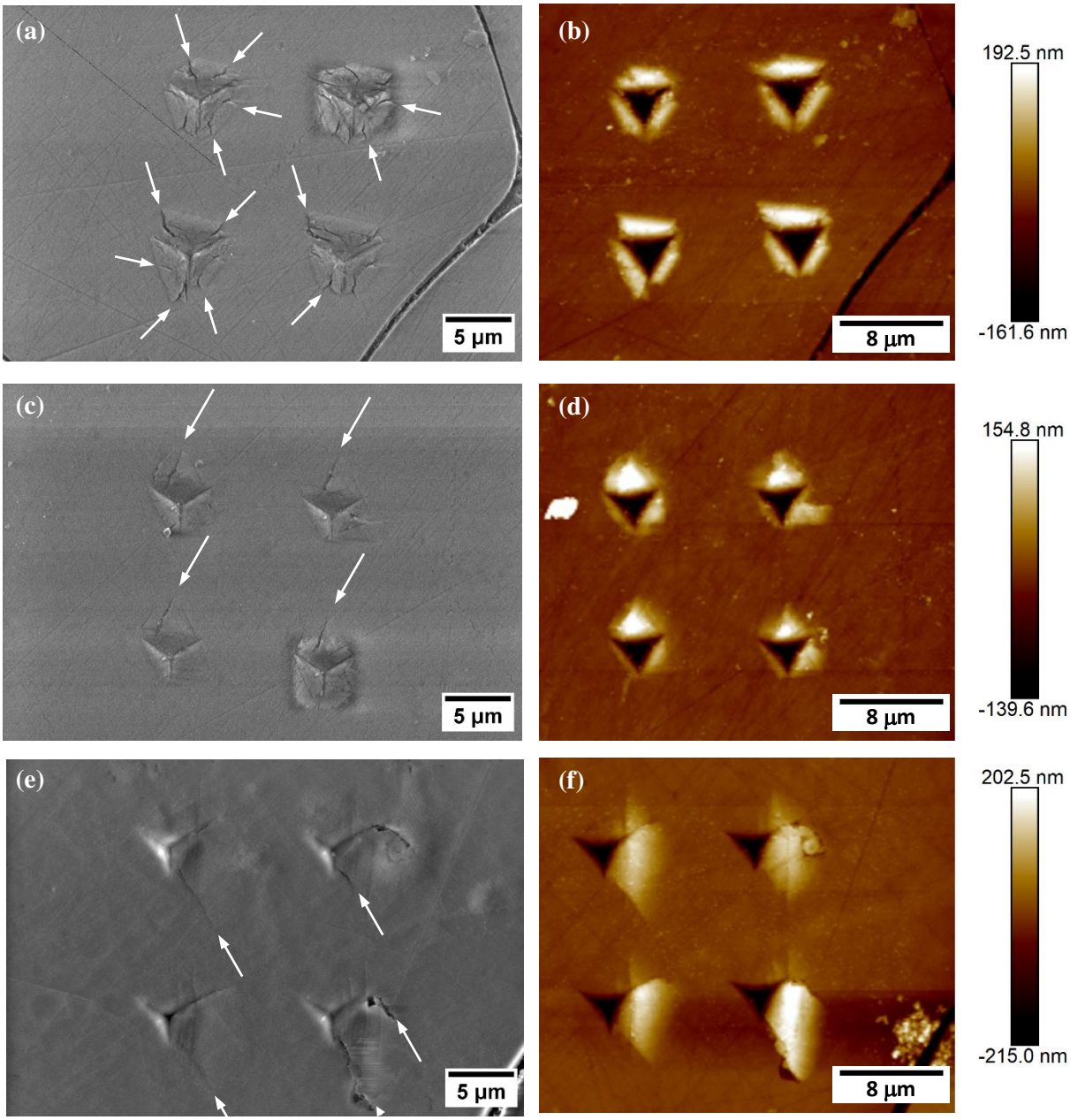

Fig. 8 Scanning electron microscopy (SEM) and atomic force microscopy (AFM) images of impressions in grains with different orientations. (a) (b) prism 4 with $c \parallel$ ND, (c) (d) inclined prism 5, (e) (f) inclined prism 6 with the plane $(1\ 0\ \bar{1}\ 4)$ nearly perpendicular to ND. The traces of the planes $\{1\ 0\ \bar{1}\ 4\}$ are indicated by arrows.

synthetic ceramics[41], the zone of plastic deformation located below the impression becomes a source of cracks that propagate to the external surface. According to theoretical analysis, a grain with the axis $c \parallel$ ND undergoes the strongest plastic deformation. This gives rise to a dense crack system. They combine to form surfaces along which portions of material adjacent to the indents' edges undergo separation. The inclined grain represented by prism 5 behaves completely differently (Fig. 8c). Individual cracks are consistently running along the traces of the $(0\ \bar{1}\ 1\ 4)$ plane deviated by an angle of 38° from the surface

(Fig. 8c). Thus, decohesion occurs at a lower depth, and in many cases is only partial. The atomic force microscopy (AFM) measurements show that the depths and areas of the impressions, as well as the heights of the material pileups, are smaller compared to grain 4 (compare Fig. 8b and Fig. 8d). The visible reduction of plastic deformation, as well as limitation of fracture processes, is induced by the prism inclination. Higher strength and fracture toughness mean that absorption of the impact energy is much lower than in the case of grain 4. This is indicated by the greater distance to which the indenter is bounced from the sample back. It amounts to 4000 nm for grain 5, whereas for grain 4 it is 3800 nm. A small group of oblique grains shows reduced fracture toughness. It is represented by prism 6, which is illustrated in Fig. 6d. Then, during unloading, tensile stresses generate lateral cracks along the easy cleavage plane $(1\ 0\ \bar{1}\ 4)$ almost perpendicular to ND. As a result, the material is chipped, which partly occurs along the plane $(1\ \bar{1}\ 0\ \bar{4})$ deviated by the large angle of 71° from the surface (Fig. 8e, f). Both the depths of impressions and the volumes of material detached from the bulk are the largest among the grains tested. Extensive damage entails significant absorption of impact energy, resulting in a shorter distance of the indenter bounce - 3600 nm.

Compression tests

Besides the identification of mechanical properties at the nano- and microscopic levels, the response at the macroscopic level was also examined. A compression test was carried out for 6 samples cut from the rib areas of the CCP layer at the places of scales (see Fig. 4b) where the prisms strongly deviate from ND. The results, in the form of the stress-strain diagram together with the compressive strengths (σ_c) determined for the individual shell specimens, are presented in Fig. 9.

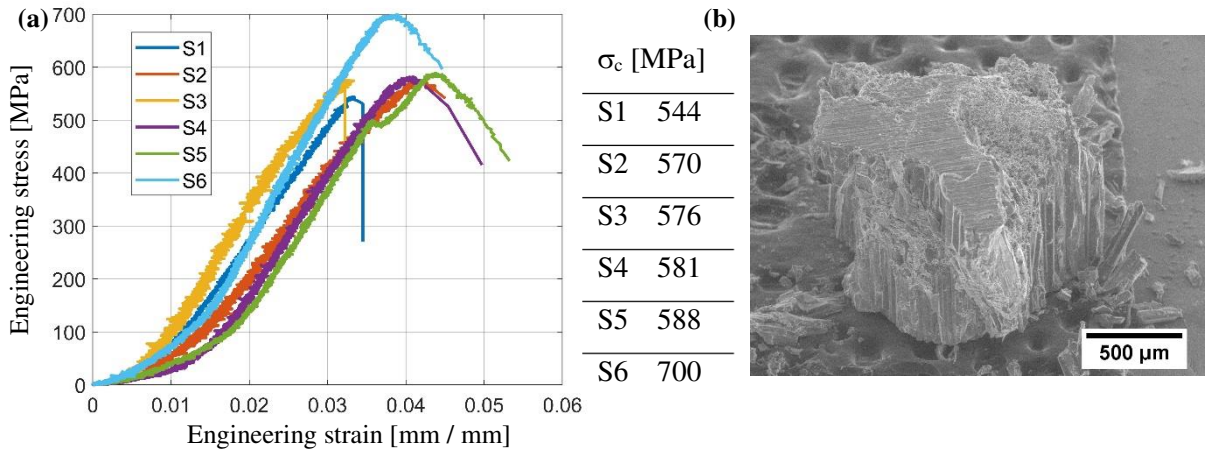

Fig. 9 Response of *Pinna nobilis* shell specimens to compression. (a) stress – strain curves together with compressive strength. (b) SEM image of specimen no. 5 after compression.

The values obtained are remarkably high considering the mechanical properties of the materials the shell is made of. Compressive strength up to 700 MPa results from the unique structure which is a weave of strong and weak units. This gives a great ability to dissipate energy and also enables blocking and delocalization of the fracture process. As a result, the loss of load capacity occurs at high stresses, when a significant part of the structure or even the entire one is destroyed. Examples of such mechanical responses are samples 5 and 6, respectively.

Conclusions

The present work focuses on radial ribs in a shell of the *Pinna nobilis* species. A specimen with a large, densely ribbed surface, generated due to a breakage at an early stage of growth, was investigated. *P. nobilis* shows a great capacity for shell reconstruction. Thus, the fracture area is distinguished only by a slightly denser arrangement of the ribs, and then they continue in a manner typical for the species under consideration. The external part of the shell is built of calcite prisms running perpendicular to the outer surface. The rib area is, naturally, strongly curved. Thus, prisms starting the growth orientate obliquely to the thickness direction. Angles between the *c*-axes of calcite grains and ND are considerable and often exceed 30°. With development, the structure is ordered and the prisms reach the nacre layer perpendicularly. Despite this, the grain crystallographic *c*-axes preserve their initial oblique orientation. The EBSD investigations reveal that the disorientation of grains is not random. Most often they rotate relative to each other around the *c*-axis by 18°, 38° and 60°. In order to uncover the reason for the

observed strong preference, the interface energy change during the continuous rotation of one grain relative to the adjacent one was calculated. The results obtained show that neighboring prisms form low-energy twin disorientations. Thanks to them, a dominant *c*-axis orientation arises at the outer surface of the shell and is then transferred deeper up to the nacre layer. The twin boundary $(0\ 1\ \bar{1}\ 0)$ generates the largest rotation around the *c*-axis - 60°. Thus, it is often located along the symmetry axis of the shell rib enabling strong curvature of the growth line while maintaining coherency of the areas on the left and right.

Calcite grains with *c*-axes significantly deviated from the thickness direction ND show unique mechanical properties. This was explained by the determined distributions of the Schmid and cleavage factors. The processes of permanent deformation and brittle fracture mainly proceed along the planes of easy slip and easy cleavage. In calcite, the role is played by one family $\{1\ 0\ \bar{1}\ 4\}$. If the angle of inclination exceeds 30°, the orientation of these planes hinders both plastic slips at the loading stage and the propagation of cracks during unloading. An exception is a small group of grains in which one of the planes $\{1\ 0\ \bar{1}\ 4\}$ is located perpendicularly to ND. Nevertheless, the specific microstructure enables blocking of the extensive crack which arises then. A perfect tool is the twin boundary $(0\ 1\ \bar{1}\ 0)$, which transforms a weak grain into a strong counterpart.

The theoretical results are confirmed by the nano-indentation test. Grains typical for Pinna nobilis with *c*-axes subparallel to ND undergo advanced plastic deformations, which leads to the lowest hardness. Inclination introduced by ribs significantly increases its value. Similarly, the impact test induces intensive fracture of the typical grains. On the surface, numerous cracks running in the radial direction and along the traces of the planes $\{1\ 0\ \bar{1}\ 4\}$ are formed. The grain inclination significantly confines the fracture process. Only single cracks are observed on the external surface. The energy dissipated then is small, which is confirmed by a significantly greater bouncing distance of the indenter than in the case of typical grains.

Samples representing rib areas with strongly tilted *c*-axes were subjected to a compression test. Their strength is surprisingly high - reaching 700 MPa. The excellent mechanical properties of the biogenic material result from the weave of strong and weak structural units. The former provides load

transfer, while the latter constitutes zones of controlled energy dissipation, which is necessary to reduce brittle fracture processes.

In summary, well-shaped ribs act as a shell's reinforcement. Their unique mechanical properties are generated by prisms with *c*-axes strongly deviated from the thickness direction. They exhibit high strength and fracture toughness. The prisms of the special orientation and their role in load transfer is revealed here for the first the first time.

Materials and Methods

Microstructure investigations. The *P. nobilis* specimen was collected in 2013 from the bay of Almyropotamos, Evia island, Central Greece. The species is strongly protected by a European Council Directive (92/43/CEE). According to Article 16 paragraph 1(d) of the Directive, the specimen was collected for the purpose of scientific research. The samples were cut along both the ribs and directions perpendicular to them so as to obtain cuboids with their bases being the outer and inner shell surfaces. The obtained blocks were separately embedded in epoxy resin. The samples were ground and polished according to standard metallographic preparation protocols: mechanical polishing with silicon carbide papers 220-7000 grit followed by 1 μm and 0.25 μm diamond suspension and a final polishing step with colloidal silica suspension for 5 min using a Struers Tegramin-25 automatic polisher. The morphology and the surface characterization of fractured shells were studied with a Keyence VHX-7000 digital optical microscope. EBSD analyses were carried out using an FEI Versa 3D scanning electron microscope (SEM) equipped with an EDAX Hikari CCD camera. Diffraction patterns were collected under low vacuum (30 Pa of H_2O) at accelerating voltage (15 kV). The obtained EBSD data were analyzed using the MTEX software[42].

Disorientation. It unequivocally defines an orientation relationship between crystallites. The disorientation is determined by the smallest angle of rotation around an axis, which transforms the reference system of one crystal into another one. Due to symmetry equivalence, a given orientation relationship between crystals can be expressed by many different angle/ axis pairs which constitute a set of misorientations.

Estimation of interfacial energy. According to the Gautam – Howe method, the overlapping intensity I is a measure of the bonding strength at the phase boundary i.e. of matching the potential fields. Thus the higher the quantity I, the lower the energy of the interface treated as a disturbance[43]. In order to determine the distribution of total overlapping intensity I, in the Cartesian system $\hat{\boldsymbol{x}} \parallel [2\ \bar{1}\ \bar{1}\ 0]$, $\hat{\boldsymbol{y}} \parallel [0\ 1\ \bar{1}\ 0]$, $\hat{\boldsymbol{z}} \parallel (0\ 0\ 0\ 1)$, two calcite crystals are considered. One of them is fixed, while the other rotates around the axis $\boldsymbol{z}$ by the angle ω. The antisymmetric domain is investigated with an accuracy of 0.1°, thus $\omega \in \langle 0°,\ 60° \rangle$. Diffraction intensity I_i was assigned to each node in the reciprocal space using the structure factor $I_i = F_i \cdot F_i^{*}$[44,45]. It is assumed that the intensity is distributed according to the Lorentzian function $s_i(r) = \frac{I_i \Gamma_i}{2\pi^2 r^2 (r^2 + \Gamma_i^2)}$, where Γ_i is half of the width at half of the maximum. Γ_i constitutes the part of the sphere radius R_i bounding a reflection. With the appropriate relation R_i/Γ_i, the intensity contained in the sphere I_{ci} is almost all of the intensity I_i assigned to a given node: $I_{ci} = \int_0^{R_i} \int_0^{2\pi} \int_0^{\pi} s_i(r) r^2 \sin\varphi \mathrm{d}\varphi \mathrm{d}\theta \mathrm{d}r = \frac{2}{\pi} \arctan\left(\frac{R_i}{\Gamma_i}\right)$. It is assumed that $\Gamma_i = \frac{R_i}{12}$, then nearly 95% of the intensity I_i is taken into account. The distribution of diffraction intensities in the reciprocal space maps the potential field of a crystal. The introduction of a phase boundary significantly disturbs the continuity of the field along a given family of planes if there is a considerable misfit between the systems of the planes in the neighboring crystallites. Thus, it is assumed that the bonding along the most densely packed planes of calcite $(1\ 0\ \bar{1}\ 4)$ is broken when the mismatch amounts to 20%. As a result, using formulas derived in[43], radii of the individual spheres are obtained as $R_i = \frac{0.1\, I_i}{d_1 I_1}$, while d_1 and I_1 are interplanar distance and intensity for the considered system of planes, respectively.

Identification of mechanical properties. Nano-indentation and nano-impact tests were carried out by means of the NanoTest Vantage system with a diamond Berkovich three-sided pyramid indenter. Indentations were made parallel to the normal direction with a maximal load of 1.5 mN. In the two regions considered, grids of 2025 impressions 1 μm apart were performed, which allows the maps of hardness and reduced Young's modulus to be obtained. The average values of the mechanical characteristics for individual grains were determined on the basis of the frequency distribution of the contact stiffness k. The k means identify prisms with different orientations as well as the boundary zone

filled with organic material. Assuming a certain standard deviation, we can distinguish points belonging to individual areas and, as a result, calculate the average H and E_r that characterize them. The Nano Tests instruments also open the possibility to conduct an impact test[46]. The Berkovich indenter was used, which was moved away from the fixed specimen to obtain an accelerating force of 0.5 mN. The amplitude of the first rebound from the sample surface was measured, which gave information about the amount of energy dissipated in the material. Atomic force microscopy (AFM) measurements were determined with a Bruker Dimension ICON XR operating in the PeakForce-QNM mode in air. Data analysis was performed using NanoScope Analysis software. At the last stage of research, the static compression test was carried out. An MTS 810 servo-hydraulic test machine, equipped with an additional 25 kN load cell and an MTS clip gauge extensometer, was used. The specimens were cut from the shell using diamantine wire and had the geometry of a rectangular prism with an average cross-sectional dimension of 2 mm and an average height (thickness) of 1.2 mm. The samples were compressed in the direction of the shell thickness under grip displacement control at a speed of 0.2 μm/s.

Appendix A. Morphology of a typical *Pinna nobilis* shell

The appearance of the examined shell, which was broken at the early stage of growth, differs insignificantly from the shell representative for the *P. nobilis* species. In order to facilitate the comparison, additional images of the external and internal surfaces of a typical specimen were created (Fig. A.1). The ribs run uninterruptedly from the narrow umbo to the broad posterior margin, are quite distinct and create a characteristic sculpture of the shell. The only difference is in the part of the posterior margin, which in this case is one whole. Nacre occupies most of the anterior half of the shell and is divided into two lobes by a narrow longitudinal sulcus. The middle part of the shell, in which the median ridge (ligament) is located, has a similar structure in both cases. The surface of the sample is characterized by large, widely spaced spines and rows of scales. Pinnoidea live partially buried to one third of their length in sediment[47]. Therefore, part of the spines on the surface can be abraded and absent in the anterior portion of the shell. This is particularly evident in adult specimens. Undamaged *P. nobilis* has scars that are formed during the degradation of the spines. The surface ribbing is similar to the damaged specimen studied in the present work.

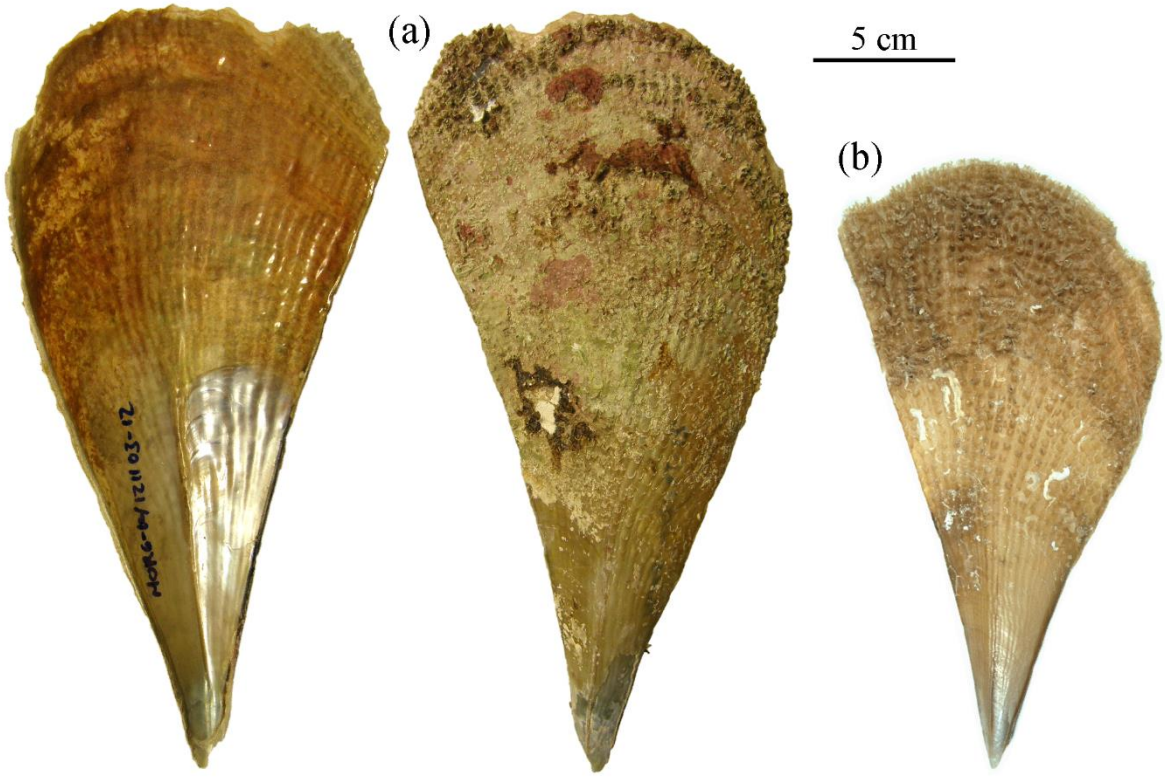

Fig. A.1. Views of typical *P. nobilis* shells. (a) Internal and external views of the left valve of an adult specimen. (b) External view of the left valve of a submature shell.

Appendix B. Arrangement of prisms subjected to nano-indentation and impact tests

The examinations were carried out in the area of the rib belonging to the posterior of the primary shell, below the fracture trace (see Fig. B.1). Basic structural units prisms grow perpendicular to the outer surface. Thus, the calcite *c*-axes of the grains runs along the radii of the rib curvature.

Fig. B.1 The location of the area in which nano-indentation and impact tests were conducted. The tested region (yellow rectangle) is in the ventral part of the left valve, below the fracture trace marked by broken yellow line.

The nano-indentation test was performed on three prisms with specific orientations (see Fig. B.2 a). The *c*-axis of the first one (G1) remains parallel to ND with an accuracy of 2° and in the next two (G2, G3) it deviates by an angle of 50°. Between grains G2 and G3 there is disorientation close to the twin relationship with respect to the plane (1 0 -1 0). Thus, the normal to the easy cleavage and slip plane (1 0 -1 4), deviated by an angle of 39° from ND in G2, undergoes rotation and forms a small angle of 9° with ND. Consequently, the grain G2 shows a high fracture toughness and the grain G3 significantly lower. The first prism G1 was initiated in the ridge of the rib (see Fig. B.2 b). As a result, the *c*-axis subparallel to ND exhibits the orientation typical of *P. nobilis* species, arising in the prevalent flat areas of the shell. Subsequent two prisms start growth in the slope of the rib. This leads to the oblique *c*-axis orientation required for units with high hardness and fracture toughness. The geometry of the outer rib surface (see Fig. B.2 b) was reconstructed on the basis of the EBSD map, where the orientations of the *c*-axes in the subsequent points of the shell were recorded with the step of 1.6 μm. A similar procedure was applied to the area subjected to the impact test (see Fig. B.3 a). The obtained outer surface shows that the dynamically loaded prisms G4, G5 and G6 are located analogously to G1, G2 and G3 (see Fig. B.3 b). As a result, the *c*-axis of the G4 grain is almost parallel to ND, the deflection angle is 1°. Grains G5 and G6 orientate obliquely, the angles between ND and the *c*-axes amount to 32° and 42°, respectively. The first of them shows high fracture toughness, while the other one significantly lower due to the location of the plane (1 0 -1 4) nearly parallel to the outer surface, the deviation angle is 4°.

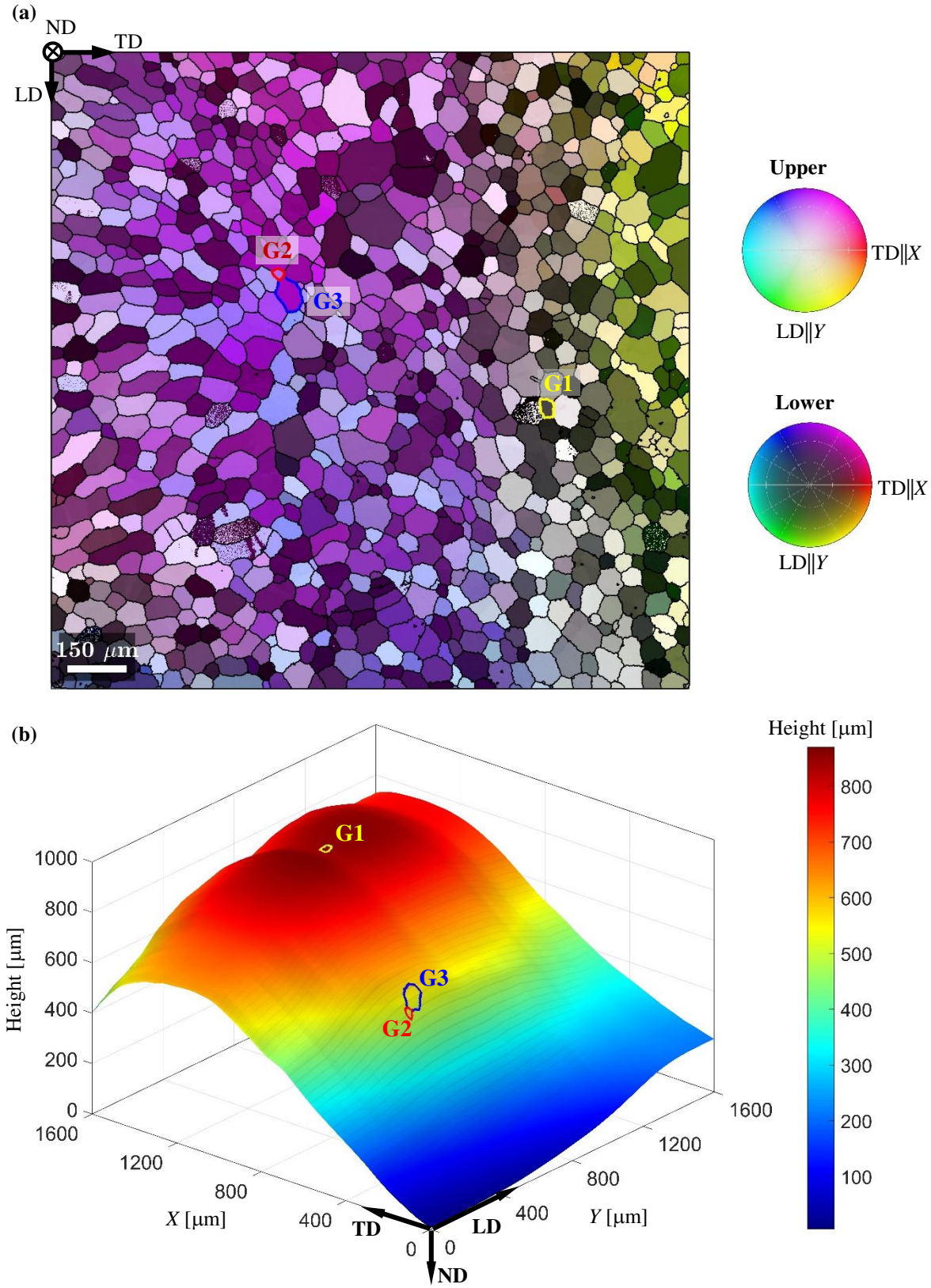

Fig. B.2 The area of the rib subjected to nano-indentation. (a) EBSD map in which grain orientation is expressed by axis/angle color coding. (b) The reconstructed geometry of the outer surface. The boundaries of the intended grains G1, G2 and G3 (see Fig. 7) are marked in yellow, red and blue, respectively.

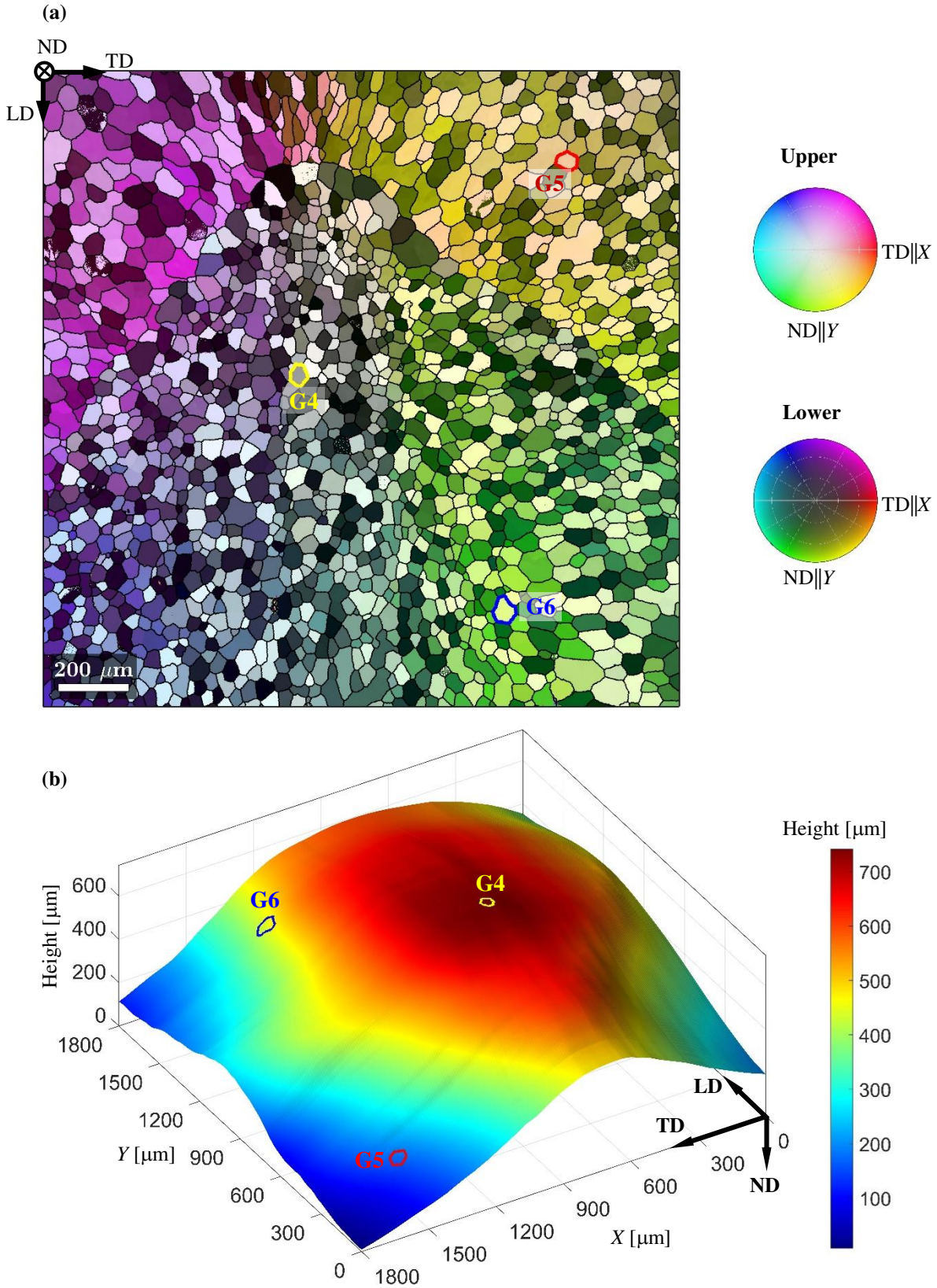

Fig. B.3 The area of the rib subjected to the impact test. (a) EBSD map in which grain orientation is expressed by axis/angle color coding. (b) The reconstructed geometry of the outer surface. The boundaries of the impacted grains G4, G5 and G6 (see Fig. 8) are marked in yellow, red and blue, respectively.

References

1. Rodriguez-Navarro, A. B., Checa, A., Willinger, M. G., Bolmaro, R., Bonarski, J. Crystallographic relationships in the crossed lamellar microstructure of the shell of the gastropod Conus marmoreus. *Acta Biomater.* **8**, 830–835 (2012).

2. Bowerbank, J. S. On the Structure of the Shells of Molluscous and Conchiferous Animals. *Trans. Microsc. Soc. London* **1**, 123–154 (1844).

3. Boggild, O. B. The shell structure of the mollusks. *Det K. Danske Vidensk. Selsk. Skr. Naturvidenskabelig og Math. Afd. Raekke 9* **2**, 231–326 (1930).

4. Volkmer, D., Harms, M., Gower, L., Ziegler, A. Morphosynthesis of nacre-type laminated CaCO3 thin films and coatings. *Angew. Chemie - Int. Ed.* **44**, 639–644 (2005).

5. Finnemore, A., Cunha, P., Shean, T., Vignolini, S., Guldin, S., Oyen, M., Steiner U. Biomimetic layer-by-layer assembly of artificial nacre. *Nat. Commun.* **3**, 1–6 (2012).

6. Xiao, Ch., Li, M., Wang, B., Liu, M.-F., Shao, Ch., Pan, H., Lu, Y., Xu, B.-B., Li, S., Zhan, D., Jiang, Y., Tang, R., Liu, X. Y., Cölfen H. Total morphosynthesis of biomimetic prismatic-type $CaCO_3$ thin films. *Nat. Commun.* **8**, 1–9 (2017).

7. Zhao, H., Yang, Z., Guo, L. Nacre-inspired composites with different macroscopic dimensions: Strategies for improved mechanical performance and applications. *NPG Asia Mater.* **10**, 1–22 (2018).

8. Schenk, S., Zlotnikov, I., Pokroy, B., Gierlinger, N., Masic, A., Zaslansky, P., Fitch, A. N., Paris, O., Metzger, T. H., Cölfen, H., Fratzl, P., Aichmayer, B. Hierarchical calcite crystals with occlusions of a simple polyelectrolyte mimic complex biomineral structures. *Adv. Funct. Mater.* **22**, 4668–4676 (2012).

9. Metzger, T.H., Politi, Y., Carbone, G., Bayerlein, B., Zlotnikov, I., Zolotoyabko, E., Fratzl, P. Nanostructure of biogenic calcite and its modification under annealing: Study by high-resolution X-ray diffraction and nanoindentation. *Cryst. Growth Des.* **14**, 5275–5282 (2014).

10. Lemer, S., González, V. L., Bieler, R., Giribet, G. Cementing mussels to oysters in the pteriomorphian tree: A phylogenomic approach. *Proc. R. Soc. B Biol. Sci.* **283**, (2016).

11. García-March, J. R., García-Carrascosa, A. M., Peña Cantero, A. L., Wang, Y. G. Population structure, mortality and growth of Pinna nobilis Linnaeus, 1758 (Mollusca, Bivalvia) at different depths in Moraira bay (Alicante, Western Mediterranean). *Mar. Biol.* **150**, 861–871 (2007).

12. Zavodnik, D., Hrs-Brenko, M., Legac, M. Synopsis on the fan shell Pinna nobilis L. in the eastern Adriatic Sea. *Les espèces Mar. à protéger en Méditerranée* 169–178 (1991).

13. Dauphin, Y. Soluble organic matrices of the calcitic prismatic shell layers of two pteriomorphid bivalves: Pinna nobilis and Pinctada margaritifera. *J. Biol. Chem.* **278**, 15168–15177 (2003).

14. Harper, E. M., Checa, A. G. Tightly shut: flexible valve margins and microstructural asymmetry in pterioid bivalves. *Mar. Biol.* **167**, 1–12 (2020).

15. Marin, F., Narayanappa, P., Motreuil, S. Acidic Shell Proteins of the Mediterranean Fan Mussel Pinna nobilis. *Prog. Mol. Subcell. Biol.* **52**, 353–395 (2011).

16. Harper, E. M., Checa, A. Physiological versus Biological Control in Bivalve Calcite Prisms: Comparison of Euheterodonts and Pteriomorphs. *Biol. Bull.* **232**, 19–29 (2017).

17. Dauphin, Y. Comparison of the soluble matrices of the calcitic prismatic layer of *Pinna nobilis*

(Mollusca, Bivalvia, Pteriomorpha). *Comp. Biochem. Physiol. - A Mol. Integr. Physiol.* **132**, 577–590 (2002)..

18. Checa, A.G., Bonarski, J.T., Willinger, M.G., Faryna, M., Berent, K., Kania, B., González-Segura A., Pina, C. M., Pospiech, J., Morawiec, A. Crystallographic orientation inhomogeneity and crystal splitting in biogenic calcite. *J. R. Soc. Interface* **10**, (2013).

19. Addadi, L., Politi, Y., Nudelman, F., Weiner, S. Biomineralization Design Strategies and Mechanisms of Mineral Formation: Operating at the Edge of Instability BT - Engineering of Crystalline Materials Properties. in (eds. Novoa, J. J., Braga, D. & Addadi, L.) 1–15 (Springer Netherlands, 2008).

20. Marin, F., Pokroy, B., Luquet, G., Layrolle, P., De Groot, K. Protein mapping of calcium carbonate biominerals by immunogold. *Biomaterials* **28**, 2368–2377 (2007).

21. Dauphin, Y., Zolotoyabko, E., Berner, A., Lakin, E., Rollion-Bard, C., Cuif, J.P., Fratzl, P. Breaking the long-standing morphological paradigm: Individual prisms in the pearl oyster shell grow perpendicular to the c-axis of calcite. *J. Struct. Biol.* **205**, 121–132 (2019).

22. Marin, F., Luquet, G., Marie, B., Medakovic, D. Molluscan Shell Proteins: Primary Structure, Origin, and Evolution. *Curr. Top. Dev. Biol.* **80**, 209–276 (2007).

23. Checa, A. G., Esteban-Delgado, F. J., Ramírez-Rico, J., Rodríguez-Navarro, A. B. Crystallographic reorganization of the calcitic prismatic layer of oysters. *J. Struct. Biol.* **167**, 261–270 (2009).

24. Sommerdijk, N., Cusack, M. Crystals competing for space. *Nat. Mater.* **13**, 1078–1079 (2014).

25. Bayerlein, B., Zaslansky, P., Dauphin, Y., Rack, A., Fratzl, P., Zlotnikov, I. Self-similar mesostructure evolution of the growing mollusc shell reminiscent of thermodynamically driven grain growth. *Nat. Mater.* **13**, 1102–1107 (2014).

26. Checa, A. G., Macías-Sánchez, E., Harper, E. M. & Cartwright, J. H. E. Organic membranes determine the pattern of the columnar prismatic layer of mollusc shells. *Proc. R. Soc. B Biol. Sci.* **283**, (2016).

27. Dauphin, Y., Brunelle, A., Medjoubi, K., Somogyi, A., Cuif, J. P. The prismatic layer of pinna: A showcase of methodological problems and preconceived hypotheses. *Minerals* **8**, (2018).

28. Jackson, A. P., Vincent, J. F. V, Turner, R. M. & Alexander, R. M. The mechanical design of nacre. *Proc. R. Soc. London. Ser. B. Biol. Sci.* **234**, 415–440 (1988).

29. Barthelat, F., Espinosa, H. D. An experimental investigation of deformation and fracture of nacre-mother of pearl. *Exp. Mech.* **47**, 311–324 (2007).

30. Rabiei, R., Dastjerdi, A. K., Barthelat, F. Interfacial Fracture Toughness of Nacre BT - Mechanics of Biological Systems and Materials, Volume 5. in (eds. Prorok, B. C. et al.) 31–38 (Springer New York, 2013).

31. Gim, J., Schnitzer, N., Otter, L.M., Cui, Y., Motreuil, S., Marin, F., Wolf, S. E., Jacob, D. E., Misra, A., Hovden, R. Nanoscale deformation mechanics reveal resilience in nacre of *Pinna nobilis* shell. *Nat. Commun.* **10**, 1–8 (2019).

32. Taylor, J. D. The mechanical properties of bivalve (Mollusca) shell structures. *Paleontology* (1972).

33. Li, X. W., Ji, H. M., Yang, W., Zhang, G. P., Chen, D. L. Mechanical properties of crossed-lamellar structures in biological shells: A review. *J. Mech. Behav. Biomed. Mater.* **74**, 54–71

(2017).

34. Strąg, M., Maj, Ł., Bieda, M., Petrzak, P., Jarzębska, A., Gluch, J., Topal, E., Kutukova, K., Clauser, A., Heyn, W., Berent, K., Nalepka, K., Zschech, E., Checa, A. G., Sztwiertnia, K. Anisotropy of mechanical properties of *Pinctada margaritifera* mollusk shell. *Nanomaterials* **10**, 634 (2020).

35. Kunitake, M. E., Mangano, L. M., Peloquin, J. M., Baker, S. P., Estroff, L. A. Evaluation of strengthening mechanisms in calcite single crystals from mollusk shells. *Acta Biomater.* **9**, 5353–5359 (2013).

36. Böhm, C. F., Feldner, P., Merle, B., Wolf, S. E. Conical nanoindentation allows azimuthally independent hardness determination in geological and biogenic minerals. *Materials (Basel).* **12**, 1–9 (2019).

37. Checa, A. G. Fabricational morphology of oblique ribs in bivalves. *J. Morphol.* **254**, 195–209 (2002).

38. Gautam, A. R. S., Howe, J. M. A method to predict the orientation relationship, interface planes and morphology between a crystalline precipitate and matrix. Part I. approach. *Philos. Mag.* **91**, 3203–3227 (2011).

39. De Bresser, J. H. P., Spiers, C. J. Strength characteristics of the r, f, and c slip systems in calcite. *Tectonophysics* **272**, 1–23 (1997).

40. Bruno, M., Massaro, F. R, Pastero, L., Costa, E., Rubbo, M., Prencipe, M., Aquilano D. New Estimates of the Free Energy of Calcite/Water Interfaces for Evaluating the Equilibrium Shape and Nucleation Mechanisms. *Cryst. Growth Des.* **13**, 1170–1179 (2013).

41. Hagan, J. T. Micromechanics of crack nucleation during indentations. *J. Mater. Sci.* **14**, 2975–2980 (1979).

42. Bachmann, F., Hielscher, R., Schaeben, H. Texture Analysis with MTEX – Free and Open Source Software Toolbox. *Solid State Phenom.* **160**, 63–68 (2010).

43. Nalepka, K., Sztwiertnia, K., Nalepka, P. Preferred orientation relationships at the Cu/α-Al2O3 interface: Identification and theoretical explanation. *Acta Mater.* **104**, 156–165 (2016).

44. Fultz, B., Howe, J. M. *Transmission Electron Microscopy and Diffractometry of Materials*. (Springer Science & Business Media, 2013).

45. E. Prince. *International Tables for Crystallography Vol. C: Mathematical, physical and chemical tables*. (Wiley, 2006).

46. Beake, B. D., Goodes, S. R., Smith, J. F. Micro-Impact Testing: A New Technique for Investigating Thin Film Toughness, Adhesion, Erosive Wear Resistance, and Dynamic Hardness. *Surf. Eng.* **17**, 187–192 (2001).

47. Garcia-March, J. R., Márquez-Aliaga, A., Carter, J. G. The duplivincular ligament of recent Pinna Nobilis L., 1758: further evidence for pterineid ancestry of the Pinnoidea. *J. Paleontol.* **82**, 621–627 (2008).

Acknowledgments

The authors thank Mr Łukasz Niedzielski from Keyence International for the possibility of performing microstructural analysis using a VHX-7000 digital microscope. Thanks to Damian Sapijaszka who collected the *P. nobilis* specimen for scientific research. The work was supported by the Polish National Agency for Academic Exchange (grant PPI/APM/2018/1/00049/U/001) and the National Science

Center (grant UMO-2018/29/B/ST8/02200). MS was supported by the European Union from the resources of the European Social Fund (Project No.WND-POWR.03.02.00-00-I043/16). AGC was funded by project CGL2017-85118-P of the Spanish Ministerio de Ciencia e Innovación. José Rafael García March (Universidad Católica de Valencia, Spain) provided the images of *Pinna nobilis* of Fig. A.1.

Author contributions

K.N., A.Ch, K.Sz., K.B. proposed and supervised the project; M.S., Ł.M. prepared the samples; K.N., K.B., T.M., A.J.H., P.N. analyzed the data and provided some experimental assistance; K.N., T.M., A.J.H. contributed to the analysis of data and mechanical measurements. K.B. performed the SEM/EBSD measurements; A. Sz. carried out the AFM measurements; KN performed calculations constituting the basis for the theoretical analysis of microstructure and mechanical properties. K.N., K.B. and A.Ch. collectively wrote the manuscript; All authors contributed to the discussion.

Competing interests: the authors declare no competing interests.

Figures

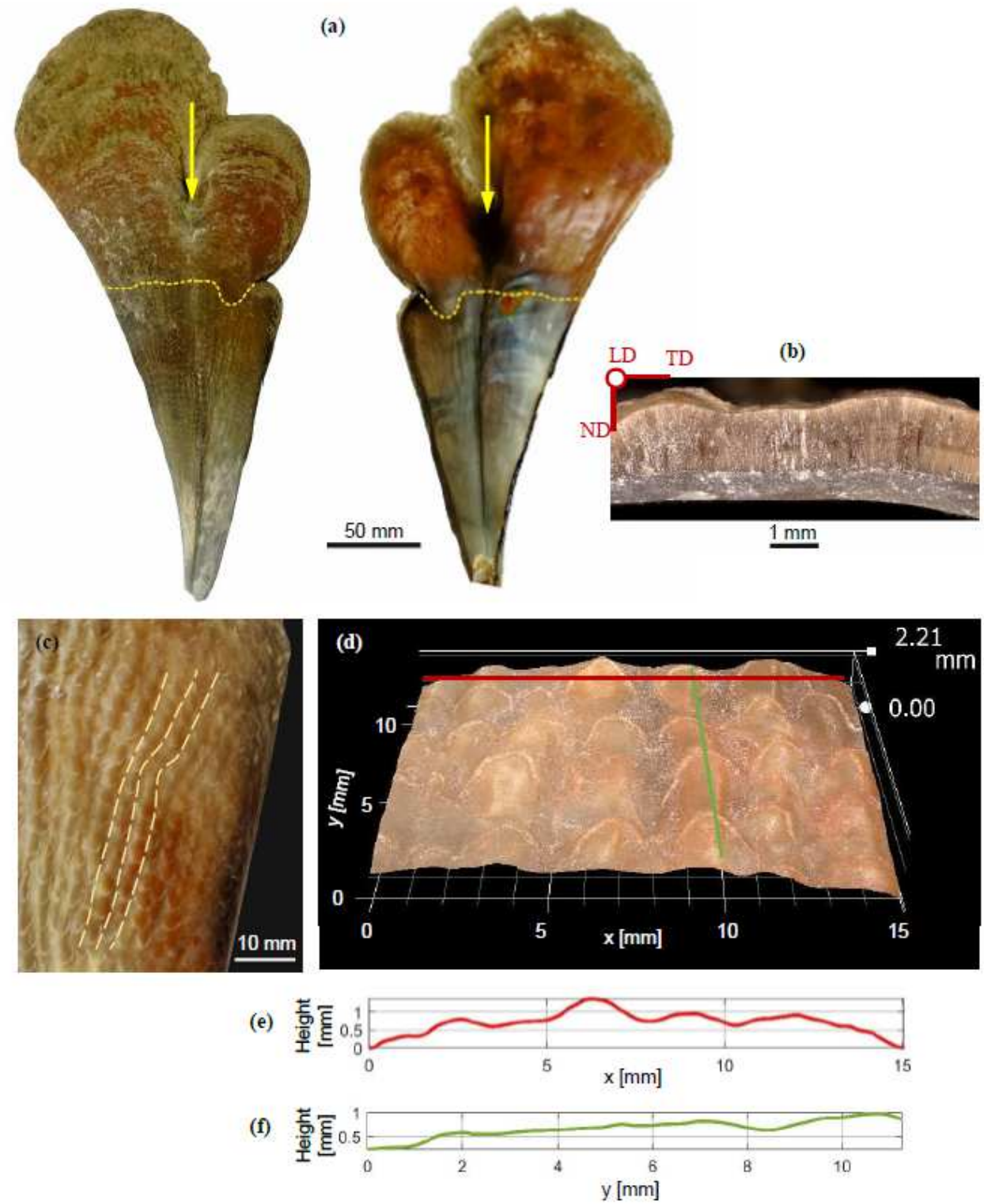

Figure 1

Morphology of Pinna nobilis shell. (a) Outer and inner view of the left valve of the specimen showing the bilobate margin produced by shell repair. The trace of the former fracture is marked with a broken yellow curve and the division lines of valves are indicated by arrows. (b) Cross-section of the shell determined by

normal (ND) and transversal (TD) directions. (c) Ribs in the ventral part. Three of them are distinguished by broken yellow lines. (d) Surface with profiles measured along (e) transversal (TD) and (f) longitudinal (LD) directions.

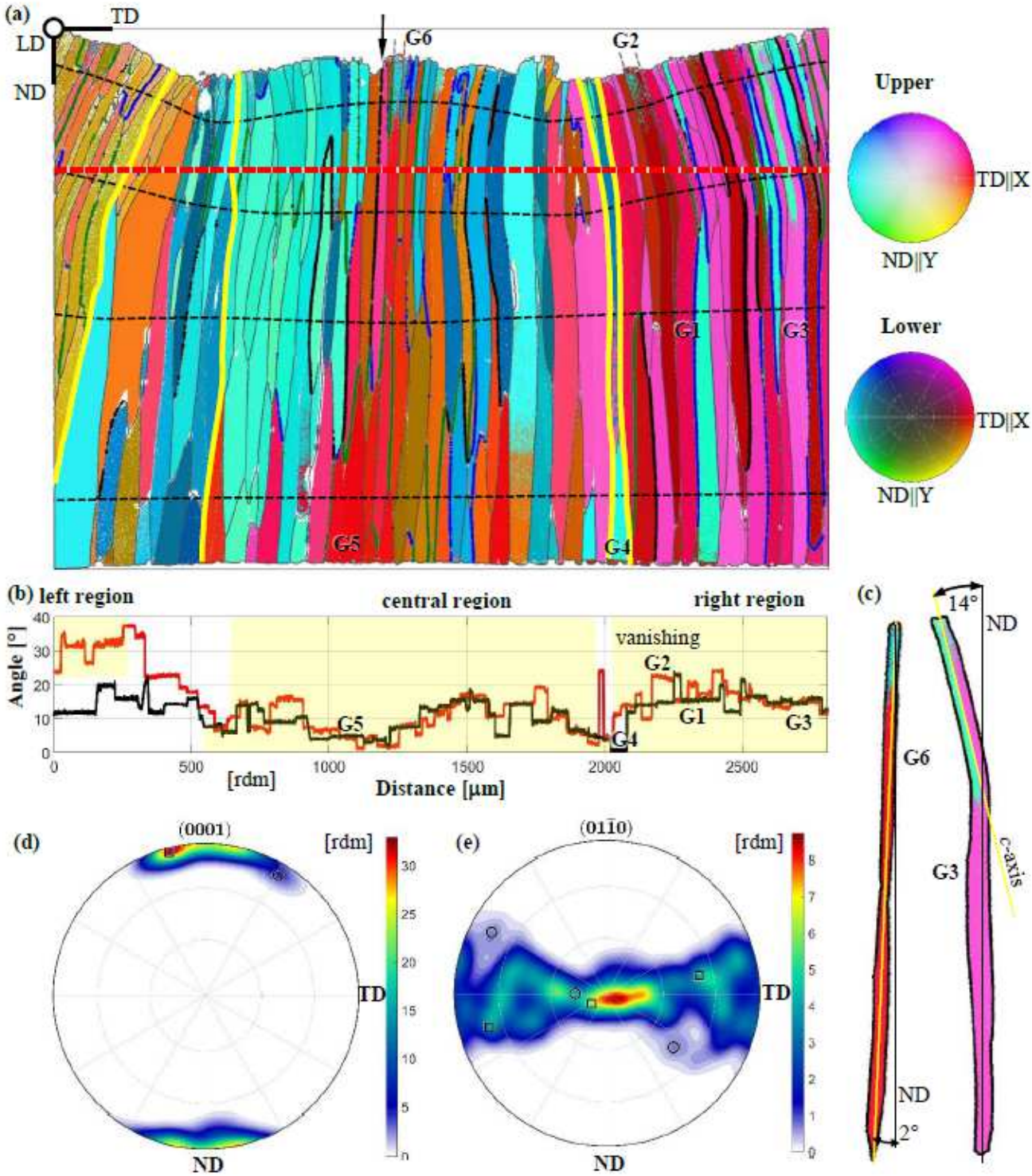

Figure 2

Microstructure of a representative cross-section through a ribbed area. (a) Orientation in axis/angle color coding. The color determines the position of the axis, while the angle of rotation is expressed by the color saturation, 0° and 90° correspond to gray and full saturation, respectively. Grains typical of P. nobilis, with

the axis c subparallel to ND, are generated through an axis with a red (e.g. G4) or blue pole (e.g. G5). Then the rotation by 90° moves the c-axis to the ND position. The regions with distinct microstructures are separated by yellow lines whereas the trace of a morphological symmetry plane is indicated by an arrow. The growth lines are denoted by black dashed lines, while boundaries with the specific disorientations A, B, C are marked in green, blue and black. (b) Angle of deviation of the c-axis from ND depending on the position determined by the level of the second (red) and the last (black) growth line. (c) Examples of grains: typical of P. nobilis and deflected. In the first case, c-axis (yellow) is subparallel to ND (d), (e) Pole distribution function (PDF) for {0 0 0 1} and {0 1 1 0} planes together with the most frequent orientations in the left (circle) and right (square) region.

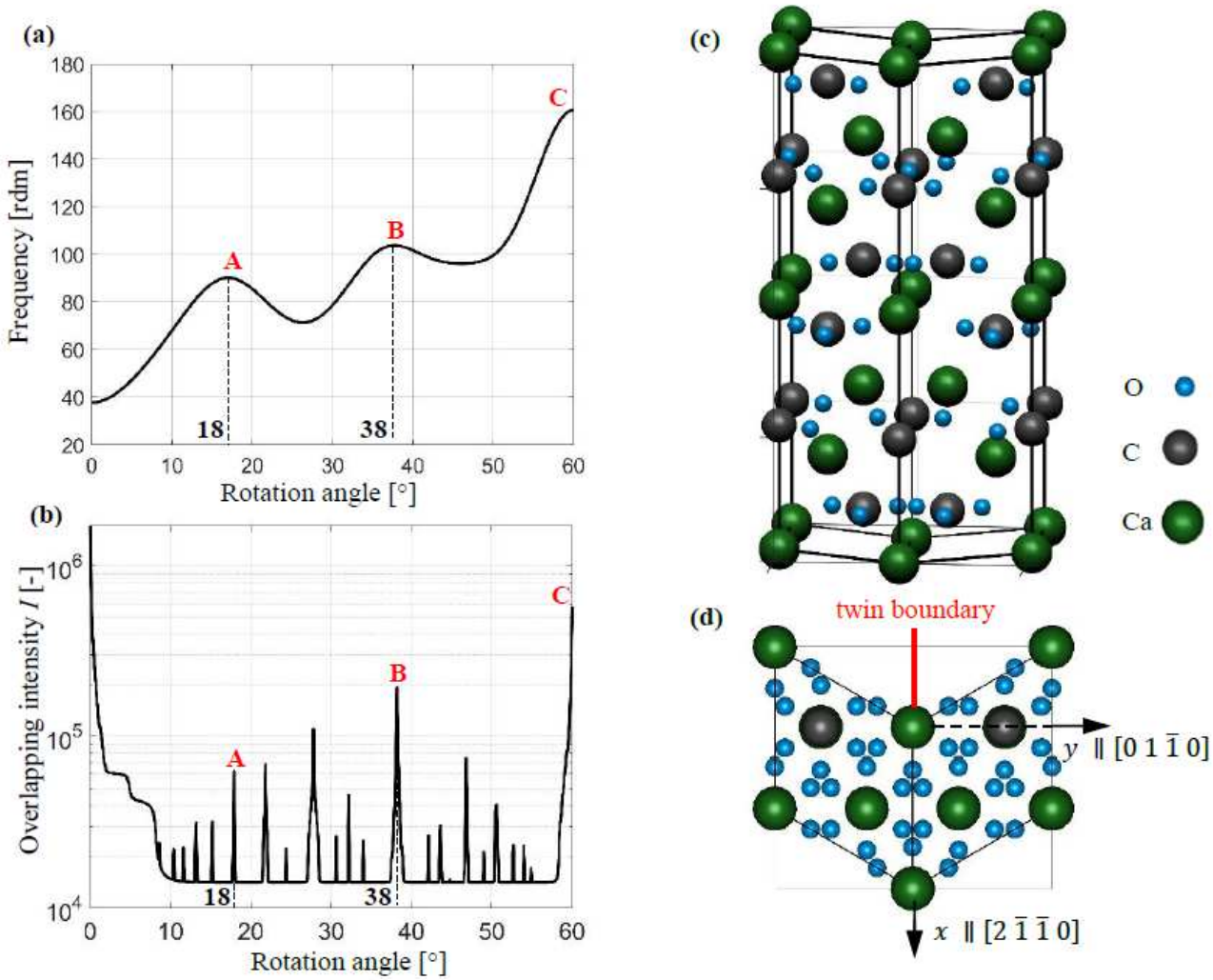

Figure 3

Preference in the misorientation of grains. (a) Distribution of disorientation angle for rotation about the c-axis showing three preferred disorientations between calcite grains of the cross-section (A, B, C) (b) Dependence of overlapping intensity I on the disorientation angle of rotation around the c-axis. The local maxima determine low-energy disorientations. (c), (d) (0 1 1 0) calcite twin.

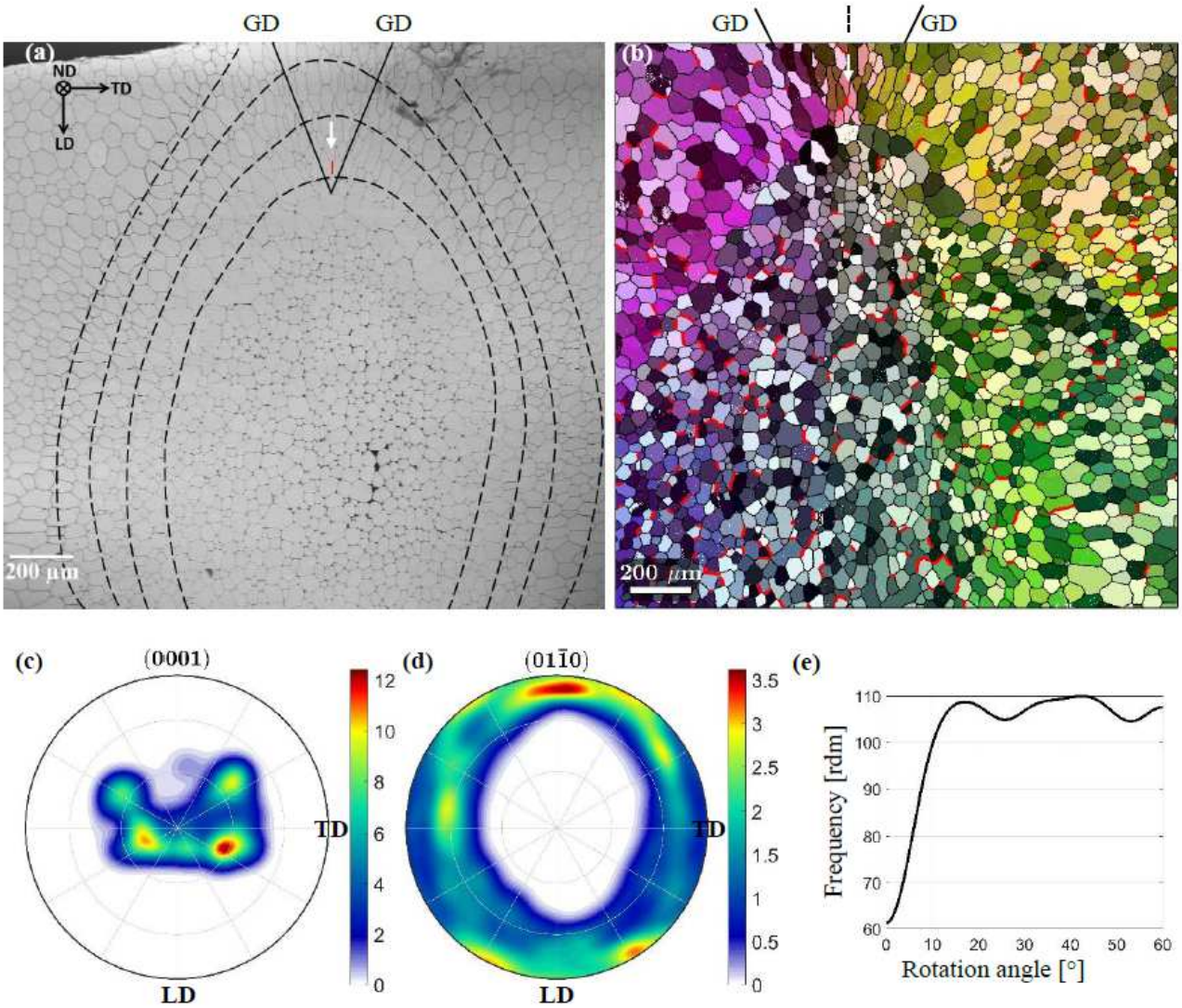

Figure 4

Microstructure of the outer shell surface. (a) SEM image with growth lines denoted by black dashed lines. (b) Grain orientation in axis/angle colour coding. Twin boundaries (0 1 1 0) are marked in red. One of them providing a smooth change in the growth direction (GD) is indicated by a white arrow. (c), (d) PDF for {0 0 0 1} and {0 1 1 0} planes. (e) Distribution of disorientation angle for rotation about c axis.

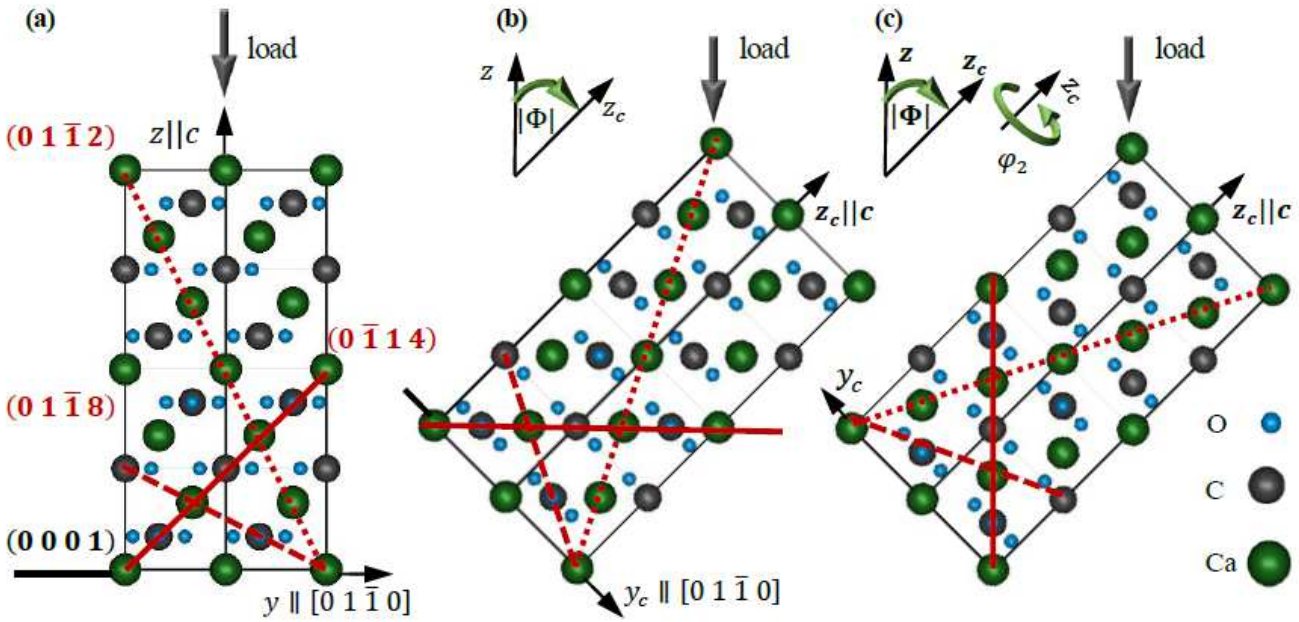

Figure 5

Typical and inclined grains. (a) Two calcite elementary cells at the initial position (b) and after rotation by the angle Φ=−45°, which is equivalent to Φ=45°,φ2=60° in an asymmetric domain of the orientation space. (c) Twin of the crystal (b), Φ=−45°,φ2=180°, which is equivalent to Φ=45°,φ2=0° in an asymmetric domain. The planes for plastic and brittle deformation are also depicted.

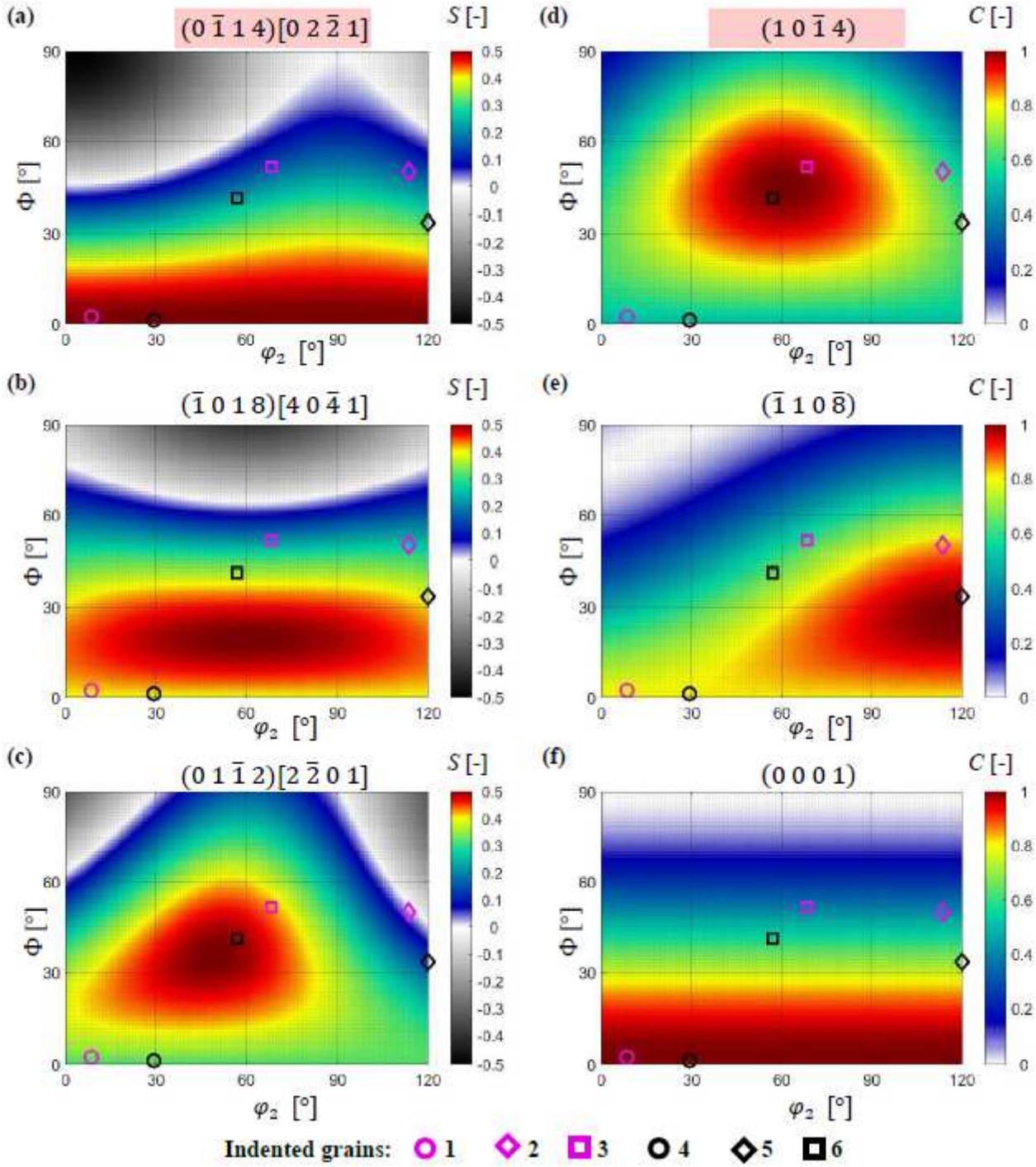

Figure 6

Schmid factor S and cleavage factor C for representative slip systems and fracture planes as functions of the crystal orientation determined by Euler angles. The relationships are presented for those slip systems and cleavage planes at which the coefficients achieve the highest values in indented grains 1–6. A positive S factor means that during unloading a positive slip arises, while at the loading stage a negative slip is generated.

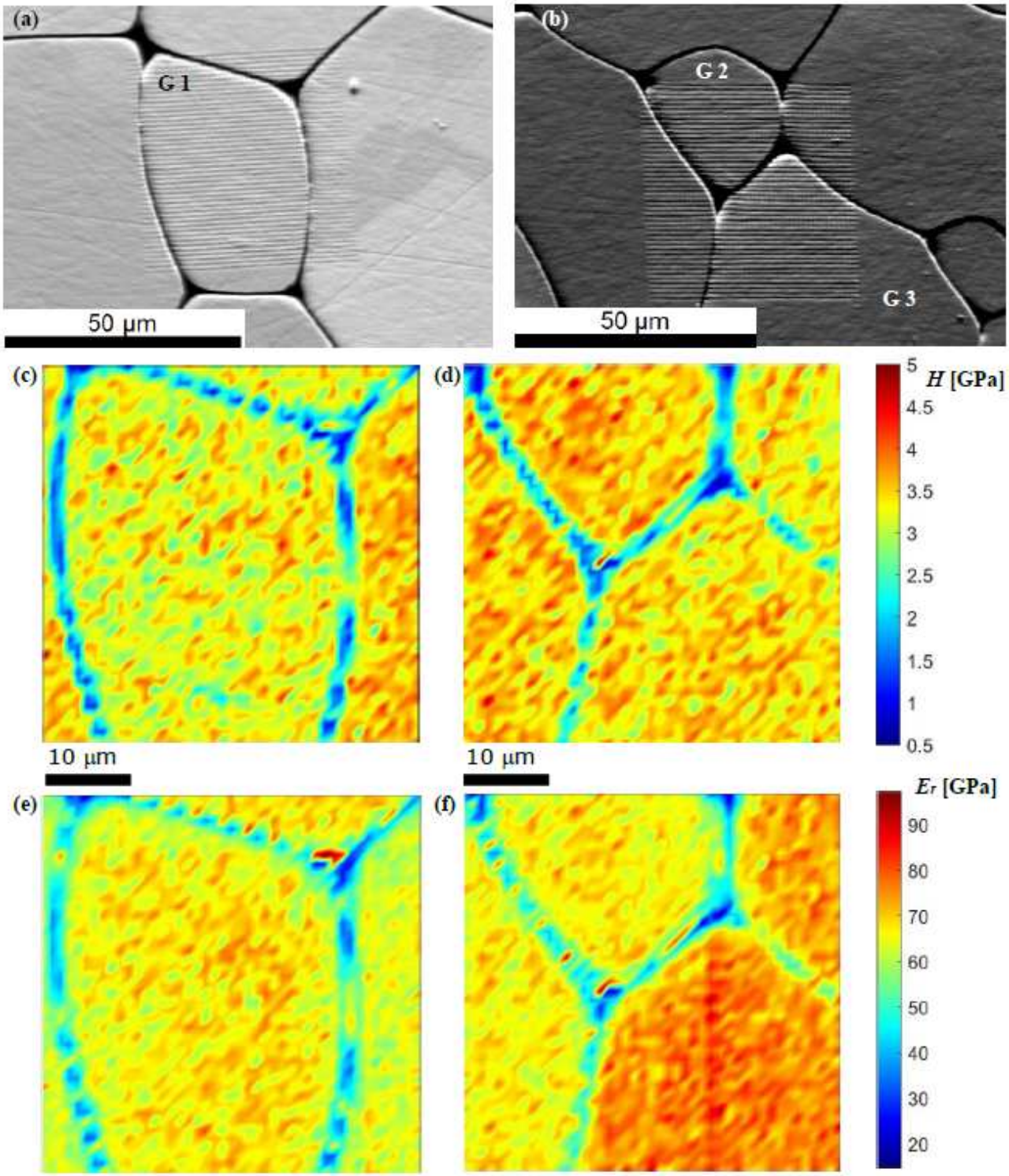

Figure 7

Nano-indentation results on individual grains. (a), (b) SEM images of the indented areas. (c), (d) hardness distribution. (e), (f) reduced elastic modulus distribution.

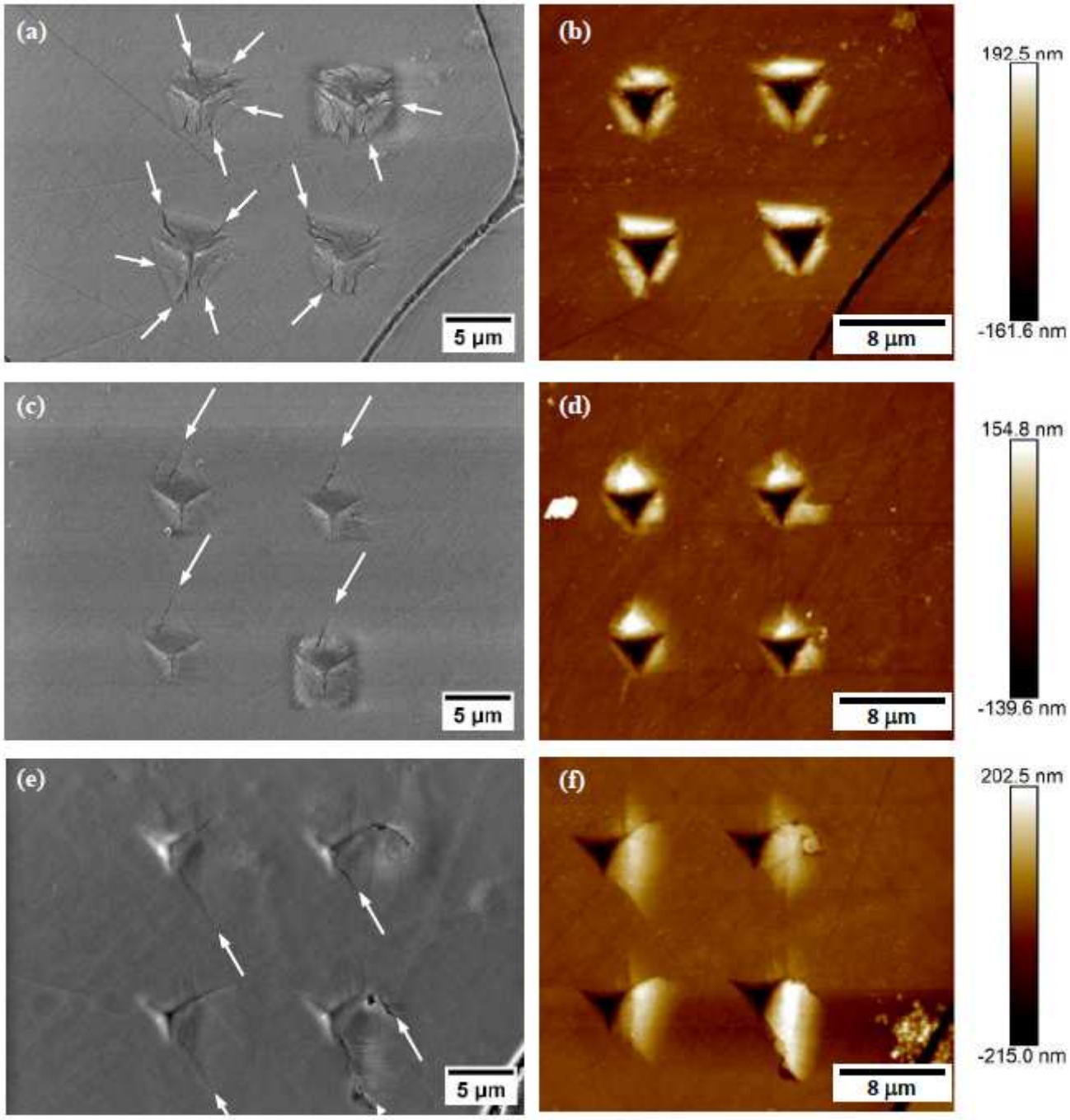

Figure 8

Scanning electron microscopy (SEM) and atomic force microscopy (AFM) images of impressions in grains with different orientations. (a) (b) prism 4 with c || ND, (c) (d) inclined prism 5, (e) (f) inclined prism 6 with the plane (1 0 1̄ 4) nearly perpendicular to ND. The traces of the planes {1 0 1̄ 4} are indicated by arrows.

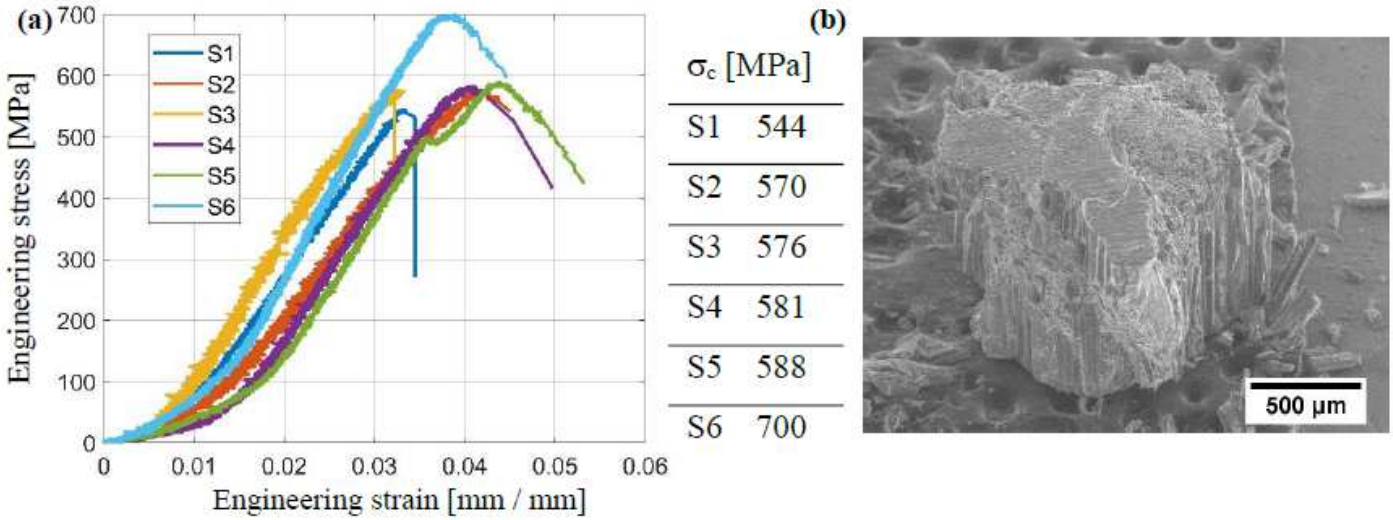

Figure 9

Response of Pinna nobilis shell specimens to compression. (a) stress – strain curves together with compressive strength. (b) SEM image of specimen no. 5 after compression.